High thermoelectric performance in Bi0.46Sb1.54Te3 nanostructured with ZnTe

Journal:	*Energy & Environmental Science*
Manuscript ID	EE-ART-01-2018-000290.R1
Article Type:	Paper
Date Submitted by the Author:	19-Mar-2018
Complete List of Authors:	Deng, Rigui; Wuhan University of Technology, State Key Laboratory of Advanced, Wuhan University of Technology Su, Xianli; Wuhan University of Technology, State Key Laboratory of Advanced Technology for Materials Synthesis and Processing; Hao, Shiqiang; Northwestern University, Materials Science Zheng, Zheng; Wuhan University of Technology, State Key Laboratory of Advanced, Wuhan University of Technology Zhang, Min; Wuhan University of Technology, State Key Laboratory of Advanced, Wuhan University of Technology Xie, Hongyao; Wuhan University of Technology, State Key Laboratory of Advanced Technology for Materials Synthesis and Processing Liu, Wei; Wuhan University of Technology, State Key Laboratory of Advanced Technology for Materials Synthesis and Processing Yan, Yonggao; Wuhan University of Technology, State Key Laboratory of Advanced Technologyfor Materials Synthesis and Processing Wolverton, Chris; Northwestern University, Department of Materials Science and Engineering Uher, Ctirad; University of Michigan, Department of Physics Kanatzidis, Mercouri; Northwestern University, Department of Chemistry Tang, Xinfeng; Wuhan University of Technology, State Key Laboratory of Advanced, Wuhan University of Technology

High thermoelectric performance in $Bi_{0.46}Sb_{1.54}Te_3$ nanostructured with ZnTe

Rigui Deng,[a] Xianli Su,[a,b*] Shiqiang Hao,[c] Zheng Zheng,[a] Min Zhang,[a] Hongyao Xie,[a]

Wei Liu,[a] Yonggao Yan,[a] Chris Wolverton,[c] Ctirad Uher,[d] Mercouri G. Kanatzidis,[b,c*]

and Xinfeng Tang[a*]

[a] *State Key Laboratory of Advanced Technology for Materials Synthesis and Processing, Wuhan University of Technology, Wuhan 430070, China*

[b] *Department of Chemistry, Northwestern University, Evanston, Illinois 60208, USA*

[c] *Department of Materials Science and Engineering, Northwestern University, Evanston, Illinois 60208, USA*

[d] *Department of Physics, University of Michigan, Ann Arbor, MI 48109, USA*

*Corresponding authors: X. Su (suxianli@whut.edu.cn), M. G. K. (m-kanatzidis@northwestern.edu), X. Tang (tangxf@whut.edu.cn).

Abstract:

Defect engineering and nano-structuring are the core stratagems for improving thermoelectric properties. In bismuth telluride alloys nanosizing individual crystallites has been extensively studied in efforts to reduce the thermal conductivity but nanostructuring with second phases has been more challenging. In this study, we demonstrate a thermoelectric figure of merit *ZT* of 1.4 at 400 K, realized in Zn-containing BiSbTe alloys (specifically $Bi_{0.46}Sb_{1.54}Te_3$) by integrating defect complexity with nanostructuring. We have succeeded in creating nanostructured BiSbTe alloys containing ZnTe nanoprecipitates. We present a melt-spinning-based synthesis that forms in-situ ZnTe nanoprecipitates to produce extremely low lattice thermal conductivity of ~0.35 $Wm^{-1}K^{-1}$ at 400 K, approaching the amorphous limit in the $Bi_{1-x}Sb_xTe_3$ system, while preserving the high power factor of $Bi_{0.46}Sb_{1.54}Te_3$. These samples show excellent repeatability and thermal stability at temperatures up to 523 K. DFT calculations and experimental results show that Zn is inclined to form dual site defects, including two substitutional defects $Zn'_{Bi/Sb}$ and a Te vacancy, to achieve full charge compensation, which was further explicitly corroborated by Positron annihilation measurement. The strong enhancement of thermoelectric properties was validated in a thermoelectric module fabricated with the melt-spun p-legs (ZnTe-nanostructured BiSbTe) and zone-melt n-legs (conventional BiTeSe) which achieved a thermoelectric conversion efficiency of 5.0% when subjected to a temperature gradient of 250 K, representing about 40% improvement compared with a commercial zone-melt-based module. The results presented here represent a significant step forward for applications in thermoelectric power generation.

Key words: BiSbTe, ZnTe, bismuth telluride, dual site defects, melt-spinning, band alignment, panoscopic approach, thermoelectricity, phase diagrams

1. Introduction

Thermoelectric materials are capable of directly converting heat into electricity and are attractive for low grade waste heat recycling and power generation[1-4]. The conversion efficiency of thermoelectric materials is governed by the dimensionless figure of merit $ZT = T\alpha^2\sigma/\kappa_{total}$, where α is the Seebeck coefficient, σ is the electrical conductivity, T is the absolute temperature, and κ_{total} is the total thermal conductivity, including both the electronic and lattice parts[5, 6]. Thus, a large Seebeck coefficient, high electrical conductivity and substantially low lattice thermal conductivity are required simultaneously to achieve an excellent thermoelectric material[7-9].

Bismuth telluride is a narrow band gap semiconductor, and its solid solutions are well-established and studied thermoelectric materials, currently dominating industrial applications because it has the highest ZT~1 near room temperature[10, 11]. In the past decade, numerous investigations were carried out to further improve its thermoelectric efficiency. Specifically, defect engineering and particle grain nanosizing have proved to be the most effective ways to regulate charge carrier and phonon transport properties[12-15].

It is well known that the thermoelectric performance of Bi_2Te_3-based solid solutions can be modulated through manipulating native defects. For example, forming a Te vacancy not only donates two electrons to the system but it also enhances the vacancy phonon scattering that lowers the thermal conductivity[16]. However, incorporating a tiny amount of extra Te in the matrix may also modulate the defect density significantly as it dramatically suppresses Te vacancies. As the content of Te increases, antisite defects of the type Te_{Sb} tend to form. Eventually, as the content of Te becomes too high, *in situ* Te secondary phases are observed that may increase rather than decrease the thermal conductivity[17]. Therefore, the density of defects, including antisites and vacancies, is controlled by a specific stoichiometry of the compound and technical processes used to synthesize it. However, a precise quantitative regulation of the defect concentration is still a challenging task, especially when using extrinsic point defects (dopants and interstitials) to optimize the thermoelectric performance[18-20] of Bi_2Te_3-based compounds. Previous studies

reported that small amount of Cu[21], Ag[22], Cd[23], and Pb[24] dopants significantly enhance the carrier concentration and reduce the lattice thermal conductivity simultaneously in p-type BiSbTe. Moreover, 1.5% Sn doping can give rise to a resonant impurity band that can significantly increase the Seebeck coefficient but higher amounts cause this effect to vanish[25].

Besides the use of defect modulation to enhance the thermoelectric performance, nanostructuring is another impactful route for achieving a significant reduction in the lattice thermal conductivity. This route is effective for strong wide-frequency phonon scattering, which under the right circumstances, can be achieved without serious deterioration of the carrier mobility. For instance, nanostructuring induced by ball-milling[26], melt-spinning[27-29], hydrothermal process[24] and texturing[30, 31] has been systematically studied over the past decade and has yielded high *ZT* values around 1.3, which is reliable and reproducible. Although defect engineering has been widely studied[12, 13, 32], the exact mechanism remains somewhat obscure and hard to quantify. By the same token, while nanostructuring by nanosizing bulk BiSbTe can yield high *ZT* values, the thermal stability and reproducibility of the structure are always a concern, particularly when elevated temperatures are the intended regime of operation.

In this study, we achieved ZnTe based nanostructures in BiSbTe alloys using a conventional synthesis method as well as a melt-spinning synthesis technique. We report a strong and reproducible enhancement of the thermoelectric performance in BiSbTe alloys via two synergistic strategies, namely, (a) suppression of thermal conductivity by forming complex combination defects including two $Zn_{Sb/Bi}$ substitutional defects and a Te vacancy, (b) refining the grain size and forming in-situ nanoprecipitation of ZnTe to further reduce thermal conductivity while preserving high power factor. Our experimental studies which are supported by theoretical calculations show that Zn prefers to substitute on Bi/Sb sites and simultaneously induces a Te vacancy on the anion site to achieve electro-neutrality. The solubility limit of ZnTe in $Bi_{0.46}Sb_{1.54}Te_3$ is significantly larger at about x = 0.06. The diversity of defects, including $Zn_{Bi/Sb}$, Te vacancy, and ZnTe nanoprecipitates dramatically

decreases the lattice thermal conductivity down to 0.62 $Wm^{-1}K^{-1}$ at room temperature for a sample with the nominal ZnTe content x = 0.06 dissolved in the $Bi_{0.46}Sb_{1.54}Te_3$ matrix using the conventional method, yet a high power factor of 4.5 $mWm^{-1}K^{-2}$ is preserved. As a result, the maximum *ZT* value reaches 1.20 at 373 K, presenting an enhancement of about 20% over the *ZT* value of pure $Bi_{0.46}Sb_{1.54}Te_3$. In order to further suppress the lattice thermal conductivity, the melt-spinning method was employed to refine the grain structure of the $Bi_{0.46}Sb_{1.54}Te_3$ matrix and *in situ*-form fine ZnTe nanoprecipitates. Such highly refined grain structure resulted in a low lattice thermal conductivity of 0.35 $Wm^{-1}K^{-1}$, close to the theoretical amorphous limit (κ_{min} = 0.31 $Wm^{-1}K^{-1}$ calculated by the Cahill's model). The melt-spun structures yielded improved thermoelectric figures of merit with the highest *ZT* value of 1.40 achieved at 400 K for a sample with the nominal dissolved ZnTe content x = 0.015. Importantly, the melt-spun samples showed excellent repeatability and thermal stability, at least at temperatures up to 523 K, after undergoing a series of specific heat treatments. Thermoelectric modules fabricated with the melt-spun p-legs and conventional zone-melt n-legs exhibited 40% performance enhancement compared with the commercial ZM-based module. Specifically a thermoelectric conversion efficiency of 5.0% was achieved under a temperature gradient of 250 K.

2. Results and Discussion

To understand the defects in the BiSbTe, Equation 1 describes the charge balance during the process of Zn doping on sites of Bi/Sb, and Equation 2 describes the charge balance in the process of dissolving ZnTe in the $Bi_{0.46}Sb_{1.54}Te_3$ matrix:

$$(x_2 + y_2)Zn_2Te_3 \xrightarrow{(Bi/Sb)_2Te_3} 2x_2 Zn'_{Bi/Sb} + 2x_2 h^{\bullet} + 3x_2 Te_{Te} + 2y_2 Zn\,Te + y_2 Te \quad (1)$$

$$(x_1 + y_1)Zn_2Te_2 \xrightarrow{(Bi/Sb)_2Te_3} 2x_1 Zn'_{Bi/Sb} + 2x_1 h^{\bullet} + 2x_1 Te_{Te} + x_1 V_{Te}^{\bullet\bullet} + 2x_1 e' + 2y_1 Zn\,Te \quad (2)$$

Based on the aforementioned presence of complex defect structures in BiSbTe alloys, the solubility limit of an extrinsic dopant is determined by the defect formation energies of the system, which in turn are affected by the strain in the lattice and the competition between electronically- and ionically-compensated reactions[7]). When the

solubility limit is exceeded, the dopant will segregate as a secondary phase. Taking this into account, we synthesized two series of Zn-containing $Bi_{0.46}Sb_{1.54}Te_3$ compounds according to the defect reactions in Eq. 1 and Eq. 2.

Figures 1(a) and 1(c) show Powder X-ray diffraction (XRD) patterns for samples of $Zn_x(Bi_{0.46}Sb_{1.54})_{1-x/2}Te_3$ (Zn is doped at Bi/Sb sites) and $Zn_xBi_{0.46}Sb_{1.54}Te_{3+x}$ (ZnTe is dissolved in $Bi_{0.46}Sb_{1.54}Te_3$) before SPS. Expanded views of the patterns between 22°-30° are shown in Figures 1(b) and 1(d). The main diffraction peaks are fully consistent with the standard pattern of $Bi_{0.5}Sb_{1.5}Te_3$ (JCPDS#01-027-1836), indicating that the main phase is $Bi_{0.46}Sb_{1.54}Te_3$. There is no obvious shift in the position of the peaks because the doping concentration of Zn or the dissolved content of ZnTe in the $Bi_{0.46}Sb_{1.54}Te_3$ matrix is relatively small. When preparing samples with the stoichiometric composition of $Zn_x(Bi_{0.46}Sb_{1.54})_{1-x/2}Te_3$ (Zn doped at Bi/Sb sites), a secondary phase of ZnTe at 25° is detected in samples with the Zn doping content $x \geq 0.015$ (marked by asterisks in Figure 1(b)), and the intensity of this peak increases notably with the increasing content of Zn. This suggests that the solubility limit of Zn in the system is around 0.01~0.015. In contrast, when preparing samples with the stoichiometric composition of $Zn_x(Bi_{0.46}Sb_{1.54})Te_{3+x}$ (ZnTe dissolved in the $Bi_{0.46}Sb_{1.54}Te_3$ matrix), the presence of the ZnTe secondary phase is detected only when one attempts to dissolve the ZnTe content *x* about 0.06. This implies that the solubility limit of ZnTe in the BiSbTe matrix is around 0.03~0.06, considerably larger than for the Zn-doped system. The larger solubility of ZnTe is due to the difference in the ratio of cations to anions (Zn:Te=1:1, Bi/Sb:Te=2:3), which gives rise to dual site defects, including two $Zn_{Sb/Bi}$ substitutional defects and a Te vacancy, as shown in Eq.2. In the case when Zn nominally substitutes on the Bi/Sb sites, no extra Te vacancies form because of the equality in the ratio of cations to anions (Zn:Te=2:3, Bi/Sb:Te=2:3) and, consequently, the solubility limit of 0.015 is low. When this solubility limit of 0.015 is exceeded, both ZnTe and extra Te secondary phases are detected. According to the electro-neutrality principle, it is likely that the presence of Te vacancies promotes the dissolution of Zn in the $Bi_{0.46}Sb_{1.54}Te_3$ matrix until the Zn content reaches 0.06, and then the ZnTe secondary phase precipitates.

Electron probe microanalysis (EPMA) measurements were carried out to investigate the phase composition of the two series of samples. For the $Zn_x(Bi_{0.46}Sb_{1.54})Te_{3+x}$ system, no contrast difference is seen on the backscattered electron (BSE) image of a sample with the ZnTe content x = 0.03 after quenching, implying a clean and homogeneous structure with no secondary phases present, see Figure 2(b). When the nominal ZnTe content x is ~0.06, a tiny amount of a secondary phase is detected and the wavelength dispersive spectroscopy (WDS) analysis shows that this secondary phase is just ZnTe. However, for the nominally Zn-doped samples, other secondary phases in addition to the ZnTe phase, appear already when $x = 0.015$ with lighter contrast. One of these other secondary phases is a rather large amount of Te, marked by a red dashed circle in Figure 2(g). The EPMA results are consistent with the XRD analysis. BSE images of the sintered bulk samples with the nominally incorporated ZnTe are shown in Figure 2(d). Corresponding BSE images for the Zn-doped samples are shown in Figure 2(h). It should be pointed out that the temperature at which the SPS compaction was carried out is higher than the melting point of Te. Consequently, a tiny amount of the Te secondary phase detected in the Zn-doped ingots after annealing has melted and was squeezed out during the SPS sintering process. As a result we could not detect any secondary phase of Te in SPS-sintered bulk samples of $Zn_x(Bi_{0.46}Sb_{1.54})_{1-x/2}Te_3$, even when the level of Zn doping was as high as x = 0.06, Figure 2(h).

The microstructure of the two series of sintered samples is shown in Figure 3 and Figure S1. For samples with the ZnTe content below 0.06, the grains with a typical layered structure are large and clean with no distinct precipitation observed. When the content of ZnTe reaches 0.06, some particles with the size ranging from several hundreds of nanometers to several microns emerge and are uniformly distributed on smooth surfaces of the matrix grains (see white particles in SEM image of Figure 3), as marked by red-dashed circles. Energy dispersive spectrometer (EDS) results indicate that these nanoparticles are ZnTe. However, for Zn-doped samples, the secondary phase of ZnTe is detected already when the content of Zn is as low as 0.015. Moreover, the quantity and the size of secondary phases are

much larger than in samples where ZnTe was dissolved in the matrix.

To understand the nature of Zn defects in the host matrix of $Bi_{0.5}Sb_{1.5}Te_3$, we evaluated various kinds of Zn-related defect formation energies using density functional theory (DFT) calculations. To account for different Zn defects, given randomly distributed Bi and Sb, we considered all 6 different Zn substitutions of Bi atom configurations in a 60 atom cell of $Bi_{0.5}Sb_{1.5}Te_3$ with the effective charge -1 (Zn_{Bi}^{1-}), 8 Zn substitutions of Sb atom configurations with the effective charge -1 (Zn_{Sb}^{1-}), 8 Te vacancies with the effective charge +2 (V_{Te}^{2+}), and 8 neutral defect complexes of $2Zn^{1-}+V_{Te}^{2+}$. Note that the defect complexes include different configurations of $2Zn_{Sb}^{1-}+V_{Te}^{2+}$, $2Zn_{Bi}^{1-}+V_{Te}^{2+}$, and $Zn_{Sb}^{1-}+Zn_{Bi}^{1-}+V_{Te}^{2+}$ and they all reside nearest neighbor sites to one another. To evaluate the relative stability of each defect complex relative to the isolated defects, we use a formation energy difference between the neutral complex and the corresponding isolated defect. For example, to evaluate the relative stability of $2Zn_{Sb}^{1-}+V_{Te}^{2+}$ compared to Zn_{Sb}^{1-} and V_{Te}^{2+}, we use $\Delta E^{form}=E_{comp}^{form}- 2E_{ZnSb}^{form} -E_{VTe}^{form}$, where E_{comp}^{form} is the formation energy of complex defect $2Zn_{Sb}^{1-}+V_{Te}^{2+}$, E_{ZnSb}^{form} refers to doping of Zn in Sb sites and E_{VTe}^{form} refers to the formation energy of the Te vacancy. Then, a negative value of ΔE^{form} suggests that the neutral complex is more favorable than the separated components and a positive value indicates that the complex is energetically unfavorable relative to separated components. We found that the formation energy differences for neutral complexes are all negative relative to the corresponding isolated defect components and range from -0.05 eV/($2Zn+V_{Te}$) to -0.41 eV/($2Zn+V_{Te}$), as shown in Table 1 and Figure 4. These results indicate that Zn defects energetically prefer to form neutral defect complexes in solid solutions of $Bi_{0.5}Sb_{1.5}Te_3$, which is consistent with the experimental results and that corroborate the presence of complex defects in the Zn doped BiSbTe alloys.

In order to make the understanding of the design idea of the experiment easier and the presentation of the actual constitution of two series of samples clearer, the proposed phase diagram of Zn-containing bismuth antimony telluride at 673 K is shown in Figure 5(a), and is based on the general knowledge of binary phase

diagrams[33, 34]. The compound of Zn_2Te_3 does not exist in reality and the red line in Figure 5(a) indicates the stoichiometric of $Zn_x(Bi_{0.46}Sb_{1.54})_{1-x/2}Te_3$ which is drawn to facilitate the presentation of this part. The related binary phases of Zn, Bi/Sb and Te are shown on the axes. In this paper, we mainly focus on a small region of the phase diagram near $(Bi/Sb)_2Te_3$ with the content of Zn below 0.12 in our two series of samples ($1^{\#}$ refers to ZnTe-incorporated samples and $2^{\#}$ refers to Zn-doped samples), enlarged in Figure 5(b). Here, six samples designated by solid symbols are chosen for detailed component analysis of the matrix by WDS. In samples with nominally dissolved ZnTe, Zn saturates at a higher content of about 2.70 than in samples where Zn is used as a dopant (about 1.40). This result is consistent with the XRD analysis that the solubility limit of Zn in $Bi_{0.46}Sb_{1.54}Te_3$ is higher when ZnTe is dissolved in the structure (x = 0.06) rather than when Zn dopes the structure (0.015).

We now turn to other structural aspects of a series of BiSbTe solid solutions that incorporate ZnTe in the crystal lattice. The lattice parameters (a-axis and c-axis) of sintered samples with different ZnTe contents are shown in Figure 6(a). When the ZnTe content is lower than 0.06, Zn atoms substitute on Bi/Sb sites and the lattice parameter along the *ab* plane decreases with the increasing ZnTe content due to the smaller radius of Zn compared to Bi/Sb. Then, as the content of ZnTe exceeds 0.06, the *a*-axis lattice parameter becomes almost constant, which signifies saturation of ZnTe in the $Bi_{0.46}Sb_{1.54}Te_3$ matrix. Meanwhile, the *c*-axis lattice parameter is almost constant since there is no intercalation between the layers. Relationships between the nominal ZnTe content and the room temperature carrier concentration and carrier mobility are shown in Figure 6(b). When Zn atoms enter into the crystal lattice, dual site defects including two $Zn_{Sb/Bi}$ substitutional defects and a Te vacancy, form. Overall, this should be electrically neutral with no contribution to the pool of charge carriers. However, it is possible that some of Sb/Bi atoms might fill Te vacancies as acceptors, increasing the concentration of holes. It is interesting to note that merely 0.1% of antisite defects $(Sb/Bi)_{Te}$ can generate 10^{19} cm^{-3} charge carriers when fully ionized. In our system, the carrier concentration slightly increases from 2.2×10^{19} cm^{-3} for the $Bi_{0.46}Sb_{1.54}Te_3$ sample to 2.8×10^{19} cm^{-3} for the $Zn_{0.03}Bi_{0.46}Sb_{1.54}Te_{3.03}$ sample.

Even though ZnTe segregates as a secondary phase when higher ZnTe content is used, the carrier concentration still increases. For instance, the carrier concentration of $Zn_{0.12}Bi_{0.46}Sb_{1.54}Te_{3.12}$ rises to about 3.5×10^{19} cm^{-3}, however, there is a distinct break in the plot of the carrier concentration as a function of ZnTe content, see Figure 6(b). The slope of the carrier concentration plot in the region of ZnTe content $0 \leq x \leq 0.03$ is much larger than in the region of higher ZnTe content ($0.06 \leq x \leq 0.12$) where ZnTe segeragates as a secondary phase. With increasing content of ZnTe, the carrier mobility decreases and seems to level off when $x > 0.03$, as illustrated in Figure 6(b). The decrease in the carrier mobility is primarily due to enhanced point defect scattering and increased carrier-carrier scattering.

Positron annihilation measurements were carried out to gain a deeper insight into the defect structure in the $Zn_xBi_{0.46}Sb_{1.54}Te_{3+x}$ system. In general, positrons can be trapped by point defects, including substitutional defects, antisite defects, and vacancies. Thus, the size and concentration of the defects can be probed *via* a variety of positron lifetimes and corresponding intensities. For polycrystalline Bi_2Te_3-based compounds, the positron annihilation spectrum can be decomposed into two lifetimes, τ_1 and τ_2, with the corresponding intensities I_1 and I_2 using the PATFIT software, see Figure 7. [35]. The positron lifetime τ_1 mostly fluctuates between 200 and 400 ps, and this represents the free positron lifetime originating from antisite defects and small vacancies. The corresponding positron annihilation intensity I_1 for our samples is more than 99% of the signal. This means that the other positron lifetime τ_2, which is longer than 1000 ps and possibly originates from grain boundaries, can be neglected[36, 37]. The positron lifetime τ_1 as a function of ZnTe content is shown in Figure 7(a). It shows a monotonously increasing trend from 312 ps for pure $Bi_{0.46}Sb_{1.54}Te_3$ to 321 ps for a sample with the nominal ZnTe content $x = 0.12$, indicating that vacancies gradually increase with the increasing ZnTe content.

Figure 8 depicts the temperature dependent electrical conductivity, Seebeck coefficient, and power factor of samples with different ZnTe content measured perpendicular to the SPS pressing direction. The electrical conductivity of all samples decreases monotonously with the increasing temperature, behaving as a highly

degenerate semiconductor. On account of the increasing carrier concentration, shown in Figure 8(c), the electrical conductivity rises with the increasing nominal ZnTe content. At room temperature, the electrical conductivity of pure $Bi_{0.46}Sb_{1.54}Te_3$ is 850 S/cm and it rises to a value of 1420 S/cm for a sample with the nominal ZnTe content $x = 0.12$. All samples exhibit positive Seebeck coefficients over the entire temperature range, documenting their p-type character with holes as the dominant charge carrier. The magnitude of the Seebeck coefficient initially increases with the temperature, approaching its maximum value near 400 K, and then decreases as intrinsic excitations start to dominate the transport. The value of the Seebeck coefficient decreases with the increasing ZnTe content, showing an inverse trend with respect to the electrical conductivity. It is noteworthy that the temperature corresponding to the peak value of the Seebeck coefficient shifts to higher temperatures with the increasing content of ZnTe. Due to the significantly enhanced electrical conductivity and only mildly decreased Seebeck coefficient, the power factor *PF* increases with the increasing ZnTe content and reaches 44.5 $\mu Wcm^{-1}K^{-2}$ at room temperature for the sample with the ZnTe content $x = 0.06$, some 20% higher power factor than the one measured for pure $Bi_{0.46}Sb_{1.54}Te_3$.

Figures 9(a) and 9(b) present the temperature dependence of the total thermal conductivity and the lattice thermal conductivity measured perpendicular to the SPS pressing direction for samples with different ZnTe contents. As the temperature increases, the total thermal conductivity of all samples initially decreases on account of the phonon Umklapp processes, reaches a minima, and then increases sharply as intrinsic excitations set in and dominates the transport process. The increased electrical conductivity contributes a significant electronic thermal conductivity term so that the value of the total thermal conductivity for a sample with the ZnTe content $x = 0.12$ reaches nearly 1.5 $Wm^{-1}K^{-1}$ at room temperature, higher than the total thermal conductivity of pure $Bi_{0.46}Sb_{1.54}Te_3$. The lattice thermal conductivities can be calculated by the Wiedemann-Franz law expressed as $\kappa_L = \kappa_t - L\sigma T$. Here, σ is the electrical conductivity, L is the Lorenz number and T is the absolute temperature. Assuming a single parabolic band model, the Lorenz number L is calculated from[38]:

$$L = \left(\frac{k_B}{e}\right)^2 \left[\frac{(r+7/2)F_{r+5/2}(\eta_F)}{(r+3/2)F_{r+1/2}(\eta_F)} - \delta^2(\eta_F)\right] \quad (4)$$

$$\alpha = \pm\frac{k_B}{e}\left[\eta_F - \frac{(r+5/2)F_{r+3/2}(\eta_F)}{(r+3/2)F_{r+1/2}(\eta_F)}\right] \quad (5)$$

$$F_i(\eta_F) = \int_0^\infty \frac{x^i dx}{1+\exp(x-\eta_F)} \quad (6)$$

where e is the elemental charge and α is the measured Seebeck coefficient. The calculated Lorenz numbers at the studied temperature range vary within the range from 1.5×10^{-8} WΩK^{-2} to 1.7×10^{-8} WΩK^{-2} for all samples with different ZnTe contents. In general, following the dissolution of ZnTe in the matrix, the resulting lattice thermal conductivity is effectively reduced, as shown in Figure 9(b). The room temperature lattice thermal conductivity as a function of the ZnTe content is displayed in Figure 9(c).

To quantify the role of alloy scattering in samples having different ZnTe content, we make use of the Callaway model[41,42]. Assuming that microstructures (grain size) of all samples are similar, the difference in the lattice thermal conductivity of various samples comes from contributions of Umklapp and point defect scattering terms only. In the Callaway model, the relation between the lattice thermal conductivity of samples with various ZnTe contents and that of the pure $Bi_{0.46}Sb_{1.54}Te_3$ solid solution (κ_L^P) can be expressed as:

$$\frac{\kappa_L}{\kappa_L^P} = \frac{tan^{-1}u}{u} \quad (7)$$

$$u^2 = \frac{\pi^2\theta_D\Omega}{h\nu^2}\kappa_L^p\Gamma \quad (8)$$

where u is the disorder scattering parameter, θ_D is the Debye temperature (155 K for $Bi_{0.46}Sb_{1.54}Te_3$), Ω is the average atomic volume (32.26×10^{-30} m^{-3} for $Bi_{0.46}Sb_{1.54}Te_3$), h is the Planck constant, v is the average sound velocity (2930 m/s for $Bi_{0.46}Sb_{1.54}Te_3$), and Γ is the scattering parameter. The scattering parameter can be calculated from the model proposed by Slack and Abeles[39, 40], $\Gamma_{calc} = \Gamma_M + \Gamma_S$, where Γ_M and Γ_S are the mass fluctuation scattering parameter and the strain field fluctuation scattering parameter, respectively. They can be written as:

$$\Gamma_M = \frac{\sum_{i=1}^n c_i\left(\frac{\overline{M}_i}{\overline{M}}\right)^2 f_i^1 f_i^2\left(\frac{M_i^1 - M_i^2}{\overline{M}_i}\right)^2}{\sum_{i=1}^n c_i} \quad (9)$$

$$\Gamma_S = \frac{\sum_{i=1}^{n} c_i \left(\frac{\bar{M}_i}{\bar{\bar{M}}}\right)^2 f_i^1 f_i^2 \varepsilon_i \left(\frac{r_i^1 - r_i^2}{\bar{r}_i}\right)^2}{\sum_{i=1}^{n} c_i} \qquad (10)$$

where n stands for the number of different atoms in the lattice and c_i are the degeneracy of atomic occupancy. For $Bi_{0.46}Sb_{1.54}Te_3$, there are two different atomic positions (Bi/Sb and Te sites), thus n = 2, $c_1 = 2$, and $c_2 = 3$. $\bar{\bar{M}}$ is the average relative atomic mass of the compound, $\bar{M}_i$ and $\bar{r}_i$ are the average atomic mass and radius on the i-th sublattice, respectively, f_i^k is the fractional occupation of the k-th atoms on the i-th sublattice, M_i^k and r_i^k are the atomic mass and radius a, respectively. The respective average quantities can be expressed as:

$$\bar{M}_i = \sum_k f_i^k M_i^k \qquad (11)$$

$$\bar{r}_i = \sum_k f_i^k r_i^k \qquad (12)$$

$$\bar{\bar{M}} = \frac{\sum_{i=1}^{n} c_i \bar{M}_i}{\sum_{i=1}^{n} c_i} \qquad (13)$$

Eqs. 7-13 can be used to predict the relationship between the lattice thermal conductivity and the ZnTe content. The results, including values of the scattering parameter, strain and mass fluctuation scattering parameters are presented in Table 2. The scattering parameter increases with the increasing ZnTe content. The mass fluctuation scattering parameter is also increasing gradually, indicating that alloying the $Bi_{0.46}Sb_{1.54}Te_3$ matrix with ZnTe causes mass fluctuations, which enhances phonon scattering. However, the value of the mass fluctuation scattering parameter is relatively small in comparison to the strain field fluctuation scattering parameter. As the ZnTe content increases, the strain field fluctuation scattering parameter increases significantly and dominates phonon scattering because of the difference in the atomic radii of Zn and Bi/Sb.

The lattice thermal conductivity behavior depicted in Figure 9(c) can be conveniently viewed as divided into three distinct regions (marked with different colors) depending on the amount and the nature/form of Zn in the $Bi_{0.46}Sb_{1.54}Te_3$ matrix. Initially (region labelled 1), Zn atoms occupy the sites of Bi/Sb and here the difference between Zn and Bi/Sb leads to significant mass and strain field fluctuations, resulting in the greatly reduced lattice thermal conductivity. The experimental data

match the Callaway model very well. In region 2, alloy scattering, on account of the presence of ZnTe, becomes weaker because the ZnTe content approaches the solubility limit of Zn in the $Bi_{0.46}Sb_{1.54}Te_3$ matrix. At the same time, a uniformly distributed small size ZnTe nanophase starts to form *in situ* in the matrix. As a consequence, the lattice thermal conductivity continues to decline, but at a considerably slower rate than in region 1. In region 3, the content of ZnTe is far beyond the solubility limit of Zn in the $Bi_{0.46}Sb_{1.54}Te_3$ matrix, ZnTe no longer dissolves in $Bi_{0.46}Sb_{1.54}Te_3$, and more and more ZnTe segregates and the volume of the nanophase grows larger. Since the thermal conductivity of this ZnTe nanophase is much higher than that of the $Bi_{0.46}Sb_{1.54}Te_3$ matrix, the lattice thermal conductivity of the composite structure increases.

To understand the impact of the morphology of nanoprecipitates on the thermal transport, we turn to the effective medium approach (EMA). According to the EMA theory[41, 42], when the secondary phase has a higher thermal conductivity than that of the matrix, the effective thermal conductivity of the composite depends on the relationship between the Kapitza radius and the distribution of particle radii. If the size of the secondary phase is smaller than the Kapitza radius, the effective thermal conductivity of the composite is reduced by interface scattering. However, dispersed particles will contribute to the effective thermal conductivity of the composite structure (considering that the sample is a physical mixture of two bulk phases). Therefore, the Kapitza radius is a critical parameter in the EMA theory, and it can be calculated as follows：

$$\alpha_k = R_{Bd} K_m \tag{14}$$

$$R_{Bd} = \frac{4}{\rho C \upsilon \eta}; \eta = pq \tag{15}$$

$$q = \frac{1}{2}\mathrm{Sin}^2\theta_c = \frac{1}{2}(v/v')^2 \tag{16}$$

$$p = \frac{4ZZ'}{(Z+Z')^2}; Z = Pv; Z' = p'v' \tag{17}$$

Here, α_k is the Kapitza radius of ZnTe particles in the $Bi_{0.46}Sb_{1.54}Te_3$ matrix, R_{Bd} is

the boundary thermal resistance, K_m, ρ, C and υ are the thermal conductivity, density, specific heat, and sound velocity of the matrix, here taken as 1.3 $Wm^{-1}K^{-1}$, 6750 $kg.m^{-3}$, 1666 $Jkg^{-1}K^{-1}$ and 2930 ms^{-1}, respectively. η is the average probability for transmission of phonons across the interface of the matrix and particles. p and q are parameters used to define η. According to the above calculation, the Kapitza radius of ZnTe particles in the $Bi_{0.46}Sb_{1.54}Te_3$ matrix is about 10 nm. Consequently, when the size of the dispersed ZnTe nanoparticles is less than 10 nm, the thermal conductivity of composite samples is reduced due to enhanced interface scattering. On the contrary, when ZnTe nanoparticles are larger than 10 nm, the thermal conductivity should increase. FESEM images of composite samples having a relatively large ZnTe content clearly show that the ZnTe secondary phase is on the scale of micrometers. That is the reason why the lattice thermal conductivity of samples with the nominal ZnTe content of $x = 0.12$ starts to show an upward trend. The minimum lattice thermal conductivity reaches ~0.62 $Wm^{-1}K^{-1}$ when the nominal content of ZnTe is 6%. This is also the ZnTe content that resulted in the optimum power factor, as noted earlier. Due to the superior electrical performance and the lower lattice thermal conductivity, the highest ZT value of 1.20 is achieved at 375 K for samples with the ZnTe content x = 0.06, representing about a 25% enhancement over the ZT value of pure state of the art $Bi_{0.46}Sb_{1.54}Te_3$.

3. Mesoscale structuring for high thermoelectric performance BiSbTe alloy

In the previous section we have shown that dissolving ZnTe into the $Bi_{0.46}Sb_{1.54}Te_3$ matrix by the conventional synthesis method of alloying/quenching/annealing can regulate the defects and phase composition so as to optimize the carrier concentration and the lattice thermal conductivity. As a result, we noted that the maximum ZT = 1.20 was achieved at 373 K for a sample with the nominal ZnTe content x = 0.06. However, the lattice thermal conductivity of this sample is still relatively high at ~0.62 $Wm^{-1}K^{-1}$, and certainly much higher than the estimated amorphous limit (κ_{min} = 0.31 $Wm^{-1}K^{-1}$) calculated by the Cahill's model[43].

Therefore, we attempted to lower the thermal conductivity by synthesizing the structure by melt-spinning (MS), which should yield a more refined grain size.

Powder XRD patterns of melt-spun ribbons of $Zn_xBi_{0.46}Sb_{1.54}Te_{3+x}$ are shown in Figure 10. For $x < 0.20$, the diffraction peaks are consistent with the standard pattern of $Bi_{0.5}Sb_{1.5}Te_3$ (JCPDS#01-027-1836) with no presence of any ZnTe secondary phase. However, when the nominal content of ZnTe exceeded 0.20, XRD detected a peak due to ZnTe at around 25°, see Figure 10(b). This value of 0.20 is much larger than that of samples prepared by the traditional method (about 0.06), as discussed above. Two possible mechanisms can be attributed to this phenomenon. On the one hand, the melt-spinning process refines grains of not only the $Bi_{0.46}Sb_{1.54}Te_3$ matrix but also the grains of the ZnTe secondary phase, and the grains may be refined to the extent that they are beyond the detection limit of XRD when $x < 0.20$. On the other hand, the highly non-equilibrium nature of the melt-spinning process increases the solubility limit of ZnTe in the system well beyond what can be achieved by conventional melting/quenching/annealing processing. This has been documented in the case of Yb-filled skutterudites synthesized by non-equilibrium processes of ball milling or melt-spinning[44, 45] and in the case of p-type PbTe-SrTe[46].

To analyze the distribution of ZnTe in the melt-spun ribbons and SPS-sintered bulks, microstructures of samples with different contents of ZnTe were characterized in detail. The contact surface (CS: ribbon's surface in direct contact with the rotating copper drum as the molten charge rapidly solidifies) and the free surface (FS) of ribbons are shown in Figures 11(a) - 11(d) and 11(e) - 11(h), respectively. The free surface shows a typical interconnected dendritic crystal with the grain size ranging from 200 - 1000 nm. The contact surface experiences a much higher rate of cooling than that of the free surface. Consequently, the grain growth on the contact surface is significantly inhibited, and the size of grains is about 100 - 200 nm. When the nominal content of ZnTe reaches 0.03, some nanoparticles with the size of about 20-30 nm emerge and are distributed uniformly on the matrix grains of the ribbons' contact surface. The quantity and size of nanoparticles increase with the increasing content of ZnTe. Apparently, larger size secondary phases are also detected at the

grain boundaries of the ribbons' free surface. EDS analysis identifies the secondary phases as ZnTe. Microstructures of the freshly-fractured surfaces of samples are presented in Figures 11(i) - 11(l) revealing lamellar structures with a typical size of about 5-20 μm. Although the grains grow somewhat during the SPS process, a large number of nanoprecipitates with an average size of around 50 nm can be found sticking to the grain boundaries, as shown in Figure 12(a). Moreover, the size of ZnTe secondary phase is greatly reduced through by melt-spinning, as can be seen in the figure 12(b). Figure 12(c-f) gives the BSE images for samples prepared by different methods and relative grain size distribution. Clearly, the grain sizes of the $Bi_{0.46}Sb_{1.54}Te_3$ matrix of the melt-spun samples are greatly refined in comparison to the grain size of samples prepared by the traditional method of melting/quenching/annealing, the average grain size of melt-spun samples is around 7 μm, less than half of the value of samples prepared by traditional method(15 μm).

Additionally, the microstructure of the bulk sample having the nominal ZnTe content x = 0.06 after the SPS processing was inspected by High-resolution transmission electron microscopy (HRTEM). Low magnification TEM images, depicting large quantities of nanoparticles with the size ranging from 10 - 200 nm randomly distributed in the matrix, are shown in Figures 13(a) and 13(b). Selected area electron diffraction (SEAD) corresponding to the $Bi_{0.46}Sb_{1.54}Te_3$ matrix is depicted in the inset of Figure 13(a). Figures 13(c) - 13(e) present HRTEM images of the area shown in Figure 13(b). In this expanded magnification, one can clearly distinguish between the matrix and the secondary phase because of the difference in their respective crystal structures and elemental composition. An image of the Fast Fourier Transform (FFT), Figure 13(f), of the secondary phase (marked by a red dashed circle in Figure 13(d) reveals that the secondary phase is ZnTe. Most nanoparticles have the size in the range 10-20 nm, close to the Kapitza radius of ZnTe in the $Bi_{0.46}Sb_{1.54}Te_3$ matrix. Therefore, such nanoparticles should be effective in enhancing interface phonon scattering and thus suppressing the thermal conductivity. Figures 13(g) and 13(h) show the Energy Dispersive Spectrometer (EDS) patterns of the matrix and the precipitated secondary phase, respectively. The data document

clearly that the matrix is $Bi_{0.46}Sb_{1.54}Te_3$ with a small Zn peak reflecting the presence of Zn substituted at Bi/Sb sites, and the precipitates are pure ZnTe. The results are fully consistent with the previous phase analysis.

In addition to the impact of nanoprecipitates on the transport behavior, the grain boundary structure is also very important regarding the charge carrier and phonon transport. Figures 13(i) and 13(j) show several typical grain boundaries in the structure. Figure 13(i) depicts grain boundaries between three adjacent grains. The upper two grains show a lattice indexed to the (0 1 5) plane, while the grain at the bottom can be indexed to the (1 0 4) plane. Figure 13(j) is another typical example of a boundary between two adjacent grains. The lattice of both grains can be indexed to the (1 1 0) plane, demonstrating a semi-coherent and low-angle grain boundary (shown as white dotted line) between two $Bi_{0.46}Sb_{1.54}Te_3$ grains. The inset in Figure 13(j) gives yet another example of a low-angle grain boundary with the phase difference between the two grains of less than 5^o. Previous studies[47] have shown that such near-perfect alignment minimizes degradation of the charge carrier mobility while it maintains its effectiveness as far as phonon scattering is concerned. Indeed, this is the reason why judiciously chosen nanostructures are effective in enhancing thermoelectric properties.

Temperature dependence of the carrier concentration obtained from Hall coefficient measurements using $n=1/eR_H$ and the carrier mobility determined from $\mu_H=\sigma/ne$ is shown in Figures 14(a) and 14(b). All samples display a weakly decreasing carrier concentration in the range 10K - 300K. As discussed previously, the carrier concentration increases with the increasing content of ZnTe, and this is also the case of melt-spun $Zn_xBi_{0.46}Sb_{1.54}Te_{3+x}$ samples. The room temperature carrier concentration here increases monotonously from 3.2×10^{19} cm^{-3} for pure $Bi_{0.46}Sb_{1.54}Te_3$ to 7.1×10^{19} cm^{-3} for a sample with the nominal ZnTe content $x = 0.06$. All samples synthesized by melt-spinning followed by SPS possess higher carrier concentration in comparison to samples with the same nominal ZnTe content but prepared by the traditional melting/quenching/annealing synthesis. The higher carrier concentration in melt-spun structures may be due to the loss of some Te during the melt-spinning process. The

higher concentration of Te vacancies would give rise to $(Sb/Bi)_{Te}$ antisite defects acting as acceptors, increasing the concentration of holes in the system. The hole mobility decreases rapidly with the increasing content of ZnTe due to enhanced scattering of charge carriers by charged point defects. As the temperature approaches 300 K, the carrier mobility of samples with the low ZnTe content follows the $T^{-3/2}$ temperature dependence, indicating the dominance of acoustic phonon scattering. As the content of ZnTe increases, alloy scattering takes gradually over and the carrier mobility instead follows the $T^{-1/2}$ dependence.

Similar to the samples prepared by the traditional method, the electrical conductivity of the melt-spun samples increases with the increasing ZnTe content. The increments in the electrical conductivity are, however, much larger than was the case of samples prepared by the traditional synthesis method. For instance, at 300 K, the electrical conductivity of the melt-spun sample having the ZnTe content x = 0.06 is about 2200 S/cm, almost two times larger than the conductivity of a sample with the same ZnTe content but prepared by the traditional synthesis, see Figure 15(a). Correspondingly, the Seebeck coefficient values near room temperature of the melt-spun samples are greatly reduced and the temperature where the Seebeck coefficient attains its maximum value shifts to much higher temperatures, as shown in Figure 15(b).

Applying the same transport analysis as in the case of samples synthesized by the traditional method, we obtained room temperature transport parameters for the melt-spun samples presented in Table 3. Figure 15(c) presents the theoretical Pisarenko plot at 300 K by assuming the effective mass $m^*=1.05\ m_e$ (m_e is the inertial mass of an electron). The Red line is the calculated one based on the two valence band model[47]. The black line is calculated based on the single parabolic band for comparison. Obviously, both lines follow closely the measured Seebeck coefficient, but the two-band model is slightly better in describing the measured Seebeck coefficient at $n>3\times10^{19}$ cm^{-3}, suggesting that all samples prepared by the traditional or the MS method possess similar m^*. This is reasonable that the presence of Zn merely shifts the Fermi level downward without notably changing the band structure near the

Fermi level. Finally, Figure 15(d) shows the temperature dependent power factor for $Zn_xBi_{0.46}Sb_{1.54}Te_{3+x}$. Due to the optimized carrier concentration, the sample with the ZnTe content x=0.015 attains the highest *PF* value of 43 $\mu Wcm^{-1}K^{-2}$ at room temperature.

Figures 16(a) and 16(b) present the temperature dependence of the total and lattice thermal conductivity of melt-spun samples with various nominal contents of ZnTe. Due to the significantly enhanced electrical conductivity, the electronic part of the thermal conductivity of melt-spun samples represents a greater fraction of the overall thermal conductivity than was the case of samples prepared by the traditional synthesis. For instance, the total thermal conductivity of a sample with the ZnTe content x = 0.06 at room temperature is as high as 1.75 $Wm^{-1}K^{-1}$, much higher than that of pure $Bi_{0.46}Sb_{1.54}Te_3$ and significantly above the thermal conductivity of the same ZnTe content sample prepared by the traditional synthesis. However, the grain size refinement achieved by the MS process remarkably reduces the lattice thermal conductivity due to much enhanced phonon scattering by high concentration of multi-scale grain boundaries and defects in the structure. In addition, the size of most of the ZnTe secondary phase precipitates in melt-spun samples is effectively decreased to 10 - 20 nm, comparable to the Kapitza radius of ZnTe in the $Bi_{0.46}Sb_{1.54}Te_3$ matrix. This, too, will boost scattering of phonons by the heterogeneous interfaces of the two phases. As a result, the minimum lattice thermal conductivity for a sample with the ZnTe content x = 0.06 is decreased to 0.35 $Wm^{-1}K^{-1}$ at 400 K, which is almost approaching the theoretical minimum lattice thermal conductivity (κ_{min} = 0.31 $Wm^{-1}K^{-1}$, calculated by the Cahill's model), and much lower than the value of the sample prepared by the traditional method with the same content of ZnTe. In a semiconductor where Umklapp phonon scattering dominates, the lattice thermal conductivity κ_L should vary as $1/T$.

The bipolar thermal conductivity κ_b[48], in the melt-spun samples becomes smaller with the increasing content of ZnTe, as shown in Figure 16(c). For instance, κ_b decreases from 0.50 $Wm^{-1}K^{-1}$ for pure $Bi_{0.46}Sb_{1.54}Te_3$ to 0.25 $Wm^{-1}K^{-1}$ for a sample with the ZnTe content x = 0.06. Moreover, for samples with the same hole

concentration (MS-0 and Quench-0.06), the bipolar thermal conductivity of melt-spun samples is much lower than those synthesized by the conventional method. The bipolar thermal conductivity κ_b is dependent on the relative position of the Fermi lever (i.e., the carrier concentration) and, for a given material, on the ratio of the minority carrier mobility to that of the majority carrier mobility. After melt-spinning, the carrier concentration of $Zn_{0.06}Bi_{0.46}Sb_{1.54}Te_{3.06}$ is much higher than that of pure $Bi_{0.46}Sb_{1.54}Te_3$. Consequently, the ratio of the majority carriers to the minority carriers has increased significantly and this inhibits the bipolar thermal conductivity κ_b. Furthermore, the size of some nanoparticles in the melt-spun samples is comparable to the minority electron wavelength, giving rise to strong preferential minority carrier scattering, which, too, diminishes the influence of the bipolar thermal conductivity. The presence of nanoprecipitates and the high concentration of grain boundaries thus not only intensifies phonon interface scattering but it also mitigates the influence of the bipolar thermal conductivity, both features being beneficial to enhancing and extending operation of thermoelectric devices. Figure 16(d) shows the temperature dependence of the figure of merit *ZT* for melt-spun samples with different contents of ZnTe. Because of their lower thermal conductivity, the melt-spun samples show enhanced *ZT* values. The highest $ZT = 1.40$ is achieved at 373 K for a melt-spun sample with the ZnTe content $x = 0.015$. The data in Figure 16(d) also show a significant shift of the peak *ZT* values to higher temperatures as the ZnTe content increases.

We have also calculated the operationally relevant average *ZT* values over the temperature range from 300 K to 500 K, which is important for practical device applications. As shown in Figure 17(a), the average *ZT* value of the pure zone-melted (ZM) $Bi_{0.46}Sb_{1.54}Te_3$ sample is around 0.65. The average *ZT* of $Bi_{0.46}Sb_{1.54}Te_3$ with the ZnTe content x = 0.06 prepared by the traditional melting/quenching/annealing synthesis is 1.10. The highest average $ZT_{Avg} = 1.20$ is achieved in melt-spun $Bi_{0.46}Sb_{1.54}Te_3$ with the ZnTe content x = 0.015. The latter two samples represent about 70%, respectively 85% enhancements over the average *ZT* of the ZM sample. In addition, compared with previous report on BiSbTe systems by others, such as ZM

BiSbTe[23], MS BiSbTe[29,50], BM ZnO/BiSbTe[20], our sample achieves optimized *ZT* value at higher temperature and wider temperature range.

The presence of nanoprecipitates and long term service of the thermoelectric module often raises concerns regarding the thermal stability and reproducibility of thermoelectric properties[49, 50]. In order to ascertain the reproducibility of high *ZT* values and the thermal stability of the samples, we repeated the same melt-spinning + SPS synthesis of $Bi_{0.46}Sb_{1.54}Te_3$ with the 1.5 mol% content of ZnTe, and cycled the samples 10 times over the temperature range 300 K to 523 K. Finally, we annealed the samples for 5 days at 523 K. The respective thermoelectric properties are shown in Figure S4, including the performance following the 10th cycle and after annealing at 523 K for 5 days. The results indicate almost unchanged transport properties upon various treatments with the maximum *ZT* values ranging between 1.32-1.42 a variation which is in the range of the experimental error of ~10%. The melt-spun samples thus have excellent reproducibility and thermal stability, at least in the temperature range up to 523 K. This bodes well for power generation applications in the medium temperature range.

To further confirm the significantly enhanced maximum and average *ZT* value of MS samples, a thermoelectric module with 71 pairs of p-n legs was fabricated with the assistance of Guangdong Fuxin Technology Co., Ltd., as shown in Figure 18(a)-(b). The fabrication details are presented in Experiment sections. The compositions of p-legs are materials prepared in this study (melt-spun samples with ZnTe content x=0.01), the n-type counterparts are commercial zone-melt $Bi_2Te_{2.7}Se_{0.3}$ single crystal provided by Guangdong Fuxin Technology Co., Ltd., its thermoelectric properties shown in Figure S5 and the performance of MS module and commercial ZM module is summarized in Figure S6 and Table S2. The power output and thermoelectric conversion efficiency of this module together with a commercial ZM-based module are shown in Figure 18(c)-(d). With the increasing temperature gradient, the maximum output power and conversion efficiency of both modules increase. When the temperature difference across the module reaches 250 K (T_{cold} = 33 □, T_{hot} = 283 □), the ZM module exhibits a maximum power output of 2.40 W and

a maximum thermoelectric conversion efficiency of 3.6%, whereas the MS module shows a maximum power output of 3.25 W, which is about 35% higher than that of ZM module. Accordingly, high thermoelectric conversion efficiencies up to 5.0% are obtained in MS module, representing a 40% improvement in comparison to that of ZM module. The enhancement of power output and conversion efficiency in the MS module is more obvious at high temperature compared with that of ZM module. These results decisively confirm the significantly enhanced maximum as well as average *ZT* of the ZnTe-nanostructured MS sample. It should be noted that the thermoelectric properties of the n-type legs in our module still remain at a relative low value in comparison with p-type legs, the compatibility of thermoelectric properties of p-n legs is also a critical issue for high performance thermoelectric modules. Further improvement of the module can be achieved by enhancing the thermoelectric properties of n-type legs.

4. Conclusions

We have realized a very high thermoelectric performance (*ZT* = 1.4 at 373 K) and high average *ZT* (ZT_{Avg}=1.20) in Zn doped and ZnTe-nanostructured BiSbTe via complex defects and microstructure modulation. Zn impurities tends to form a charge compensated dual site defects character where two Zn substitute on Bi/Sb sites accompanied with forming Te vacancy simultaneously to achieve an electro-neutrality. Zn induced complex combination defects in the crystal lattice of $Bi_{0.46}Sb_{1.54}Te_3$ results in significant mass and strain field fluctuations, both of which dramatically enhance phonon point defect scattering and reduce the lattice thermal conductivity. With the power factor *PF* = 45 $\mu Wcm^{-1}K^{-2}$ and the low lattice thermal conductivity κ_l = 0.62 $Wm^{-1}K^{-1}$ measured on a sample with the nominal ZnTe content x = 0.06, the maximum *ZT* value reached 1.20 at 373 K, an enhancement of about 20% over pure $Bi_{0.46}Sb_{1.54}Te_3$.

To further suppressing the thermal conductivity, we synthesized the ZnTe containing $Bi_{0.46}Sb_{1.54}Te_3$ by melting spinning to refine grains size of the matrix with in situ formed ZnTe nanoprecipitates. As a consequence of much enhanced phonon boundary scattering, the exceptionally low lattice thermal conductivity of ~0.35

$Wm^{-1}K^{-1}$, close to the theoretical amorphous limit (κ_{min} ~ 0.31 $Wm^{-1}K^{-1}$) was measured at 425 K on a sample with the ZnTe content x = 0.06. The melt-spun samples possess excellent repeatability and thermal stability at temperatures up to 523 K. Moreover, the thermoelectric module fabricated with the melt-spun p-legs and zone-melt n-legs produces the largest thermoelectric conversion efficiency of 5.0% under the temperature gradient of 250 K, representing about 40% enhancement over the commercial ZM-based module. This gives confidence that the melt-spun Zn-containing $Bi_{0.46}Sb_{1.54}Te_3$ structures should be suitable for high performance thermoelectric power generation applications near room temperature.

5. Experimental section

Conventional method of synthesis: high-purity Bi (5N), Sb (5N), and Te (5N) granules were weighed according to the stoichiometric composition of $Zn_xBi_{0.46}Sb_{1.54}Te_{3+x}$ (nominal ZnTe content *x* dissolved in the $Bi_{0.46}Sb_{1.54}Te_3$ matrix, x =0, 0.005, 0.01, 0.015, 0.03, 0.06, 0.12) and $Zn_x(Bi_{0.46}Sb_{1.54})_{1-x/2}Te_3$ (nominal amount *x* of Zn doped at the Bi/Sb sites, x =0, 0.005, 0.01, 0.015, 0.03, 0.06, 0.12), and loaded into vacuum-sealed quartz tubes with the inner diameter of 15 mm. The charge was melted and homogenized in a rocking furnace for 10 h at 1073 K and then quenched into supersaturated salt water. The obtained ingots were further annealed at 673 K for 5 days, and then hand-ground into fine powders, and finally compacted with the aid of spark plasma sintering (SPS) apparatus at 723 K for 5 min under 30 MPa. The fully condensed bulk ingots with the relative density over 99% were obtained with the diameter of 12.7 mm and the height of 13 mm. For a typical experiment the following amounts were used: Bi (1.8432 g), Sb (3.5952 g), Te (7.4864 g,), and Zn (0.0752 g) to prepare a 13 g ingot of $Zn_{0.06}Bi_{0.46}Sb_{1.54}Te_{3.06}$, and Bi (1.8645 g), Sb (3.6365 g), Te (7.4798 g), and Zn (0.0192 g) to prepare a 13 g ingot of $Zn_{0.015}(Bi_{0.46}Sb_{1.54})_{0.9925}Te_3$.

The melt-spinning process: ingots of $Zn_xBi_{0.46}Sb_{1.54}Te_{3+x}$ (nominal ZnTe content *x* dissolved in the $Bi_{0.46}Sb_{1.54}Te_3$ matrix, x =0, 0.005, 0.01, 0.015, 0.03, 0.06) prepared by the above described traditional melting/quenching process were inserted into

quartz tubes with a 0.3 mm diameter nozzle at the bottom and mounted on a melt-spinning apparatus. The chamber was filled with Ar (0.04 MPa) to protect the ingot from oxidation while the charge was RF melted. The melt was ejected under a pressure pulse of 40 kPa of Ar onto a copper roller rotating with a linear speed of 20 ms^{-1}. Thin ribbons (5-10 μm in thickness, 2 mm in width and 5-10 mm in length) were obtained *via* an ultra-fast solidification process with the yield of about 90%. The melt-spun ribbons were hand-ground into fine powders and compacted using the same SPS process described above. For a typical experiment, the following amounts were used: Bi (1.8671 g), Sb (3.6419 g), Te (7.4720 g), and Zn (0.0191 g) to prepare a 13 g ingot of $Zn_{0.015}Bi_{0.46}Sb_{1.54}Te_{3.015}$. In order to ascertain the reproducibility and the thermal stability of the samples, we repeated the same melt-spinning + SPS synthesis of $Zn_{0.015}Bi_{0.46}Sb_{1.54}Te_{3.015}$, and cycled the samples 10 times over the temperature range 300 K to 523 K. Finally, we annealed the samples for 5 days at 523 K. No significant changes in the properties were observed.

Structure characterization & Microscopy: The phase composition of bulk samples was identified by the Powder XRD analysis (PANalytical–Empyrean; Cu Kα). Composition and morphology of the bulk samples was investigated by electron-probe microanalysis with wavelength-dispersive spectroscopy (EPMA, JXA-8230, JEOL, Japan), field-emission scanning electron microscopy (FESEM, Hitachi SU-8020, Japan), and high-resolution transmission electron microscopy (HRTEM, JEM-2100F, JEOL, Japan) equipped with an energy-dispersive spectroscope to determine the actual composition. Positron lifetime spectra were measured using a conventional fast −fast coincidence system with a time resolution of about 220 ps, and a ^{22}Na positron source with the intensity of about 20 μCi was used. All tests were performed on samples oriented perpendicular to the pressing direction of SPS.

Thermoelectric properties measurement: The electrical conductivity, σ, and the Seebeck coefficient, α, were measured simultaneously by a standard four-probe method (ZEM-3, Ulvac-Riko, Japan). The total thermal conductivity was calculated

from $\kappa = DC_p\rho$, where D is the thermal diffusivity obtained by the laser flash method (LFA-457, Netzsch, Germany), C_p is the specific heat measured by a differential scanning calorimeter (DSC Q20, TA Instruments, USA), and ρ is the density determined by the method of Archimedes. The carrier concentration and the Hall mobility were measured using a Physical Property Measurement System (PPMS, Quantum Design, San Diego, CA, USA), where $n = 1/eR_H$ and $\mu_H = \sigma/ne$. The values of D for all the samples and C_p for typical MS samples with ZnTe $x = 0.015$ in this study can be found in Supplementary Fig. S2 and S3. The measured heat capacity C_p results from both PPMS system and DSC system are close to the value calculated by Dulong-Petit law (0.190 $Jg^{-1}K^{-1}$). And all samples prepared by conventional and MS methods show quite similar C_p. In order to avoid underestimating the thermal conductivity, we set C_p as a constant of 0.197 $Jg^{-1}K^{-1}$ in the whole temperature for the calculation of thermal conductivity. The measured density of all samples range from 6.58 gcm^{-3} to 6.70 gcm^{-3} and is summarized in Supplementary Table S1. Uncertainties in the electrical conductivity, Seebeck coefficient and thermal conductivity are ±3%, ±2% and ±5%, respectively, leading to ~ 10% uncertainty in ZT.

DFT Calculations: The total energies and relaxed geometries were calculated by DFT within the generalized gradient approximation of the Perdew-Burke-Ernzerhof exchange correlation functional with Projector Augmented Wave potentials[51]. We used periodic boundary conditions and a plane wave basis set as implemented in the Vienna *ab initio* simulation package[52]. The total energies were numerically converged to approximately 1meV/cation with spin-orbit coupling using a basis set energy cutoff of 500 eV, and dense k-meshes corresponding to 4000 per reciprocal atom k-points in the Brillouin zone. It is well known[53] that $(Bi,Sb)_2Te_3$ crystallizes with the trigonal structure in the R-3m space group where Bi and Sb share Sb sites in Sb_2Te_3 as a solid solution. We then used a special quasi-random structure (SQS)[54] of $Bi_{0.5}Sb_{1.5}Te_3$ in a 60 atom supercell to represent the solid solution of $(Bi,Sb)_2Te_3$. The SQSs are ordered structures with a relatively small unit cell, with atoms placed on lattice sites in such a way as to mimic the pair and multi-body correlations of a perfectly random lattice.

SQSs allow one to treat random solid solutions at the DFT-level, including the important physical effects of local atomic relaxation, without the computational cost of configurationally averaging a large supercell.

Module fabrication: TE modules with the size of 30×30×3.8 mm^3 and a total 71 pairs of p-n legs were fabricated with the assistance of Guangdong Fuxin Technology Co., Ltd. The size for the legs is 1.4×1.4×2 mm^3. Copper is used as electrode and nickel is chosen as diffusion barrier to inhibit element diffusions and chemical reactions between TE materials and solder. The compositions of p-legs are materials prepared in this study (melt-spun samples with ZnTe content x=0.01), the n-type counterparts are commercial zone-melt $Bi_2Te_{2.7}Se_{0.3}$ single crystal provided by Guangdong Fuxin Technology Co., Ltd. The n type and p type materials used for Zone melting module are commercial zone-melt $Bi_2Te_{2.7}Se_{0.3}$ and $Bi_{0.5}Sb_{1.5}Te_3$ single crystals, respectively provided by Guangdong Fuxin Technology Co., Ltd. The power outputs and TE conversion efficiencies of these modules were evaluated by using commercial PEM-2 testing system (ULVAC-RIKO, Inc.).

Supplementary Information

Electronic supplementary information (ESI) is available online.

Conflicts of interest

There are no conflicts to declare.

Author contribution

R. D. and X. S. conceived of and planned the experiments. R. D., H. X. and Z. Z. prepared the samples, and carried out thermoelectric experiments. M. Z. conducted EPMA measurement of the samples. R. D. and Y. Y. measured the conversion efficiency of the devices. S. H. and C. W. carried out the DFT calculations. W. L. helped with sample synthesis. R. D., X. S., C. U., M.G.K. and X. T. interpreted all results and wrote and edited the manuscript. All authors have

reviewed, discussed and approved the results and conclusions of this article.

Acknowledgements

The authors thank Rong Jiang, Tingting Luo and Meijun Yang for help with the HRTEM analysis and EPMA measurement, and Zhiquan Chen from Wuhan University for help with Positron annihilation measurement. The authors wish to acknowledge support from the Natural Science Foundation of China (51402222, 51521001, and 51632006), the Fundamental Research Funds for the Central Universities (WUT: 162459002, 2015□061) and the 111 Project of China (Grant No. B07040). At Northwestern University (X. S., S. H., C. W. and M. G. K.), thermoelectric property measurements and DFT calculations were supported by a grant from the U.S. Department of Energy, Office of Science, and Office of Basic Energy Sciences under Award Number DE-SC0014520.

References

1. L. E. Bell, *Science*, 2008, **321**, 1457.
2. J. He and T. M. Tritt, *Science*, 2017, **357**, eaak9997.
3. G. Tan, L. D. Zhao and M. G. Kanatzidis, *Chem. Rev.*, 2016, **116**, 12123-12149.
4. D. Zhao and G. Tan, *Appl. Therm. Eng.,* 2014, **66**, 15-24.
5. H. J. Goldsmid, *Introduction to Thermoelectricity*, 2016, **121**, 339–357.
6. S. LeBlanc, S. K. Yee, M. L. Scullin, C. Dames and K. E. Goodson, *Renew. Sust. Energ. Rev.*, 2014, **32**, 313-327.
7. W. G. Zeier, A. Zavalkink, Z. M. Gibbs, G. Hautier, G. J. Snyder. and M. G. Kanatzidis, *Angew. Chem. Int. Ed.*, 2016, 2-18.
8. M. Beekman, D. T. Morelli and G. S. Nolas, *Nat. Mater.*, 2015, **14**, 1182-1185.
9. H. Alam and S. Ramakrishna, *Nano Energy*, 2013, **2**, 190-212.
10. H. Mun, S. M. Choi, K. H. Lee and S. W. Kim, *ChemSusChem*, 2015, **8**, 2312-2326.
11. O. G. K. L. E. Shelimova, P. P. Konstantinov, E. S. Avilov, and a. V. S. Z. M. A. Kretova, *Inorg. Mater.,* 2003, 451-460.
12. T. Plecháček, J. Navrátil, J. Horák and P. Lošťák, *Philos. Mag.,* 2004, **84**, 2217-2228.
13. Y. Liu, M. Zhou and J. He, *Scripta Mater.*, 2016, **111**, 39-43.
14. W. Liu, X. Yan, G. Chen and Z. Ren, *Nano Energy*, 2012, **1**, 42-56.
15. Y. Wu, S. W. Finefrock and H. Yang, *Nano Energy*, 2012, **1**, 651-653.
16. T. Zhang, J. Jiang, Y. Xiao, Y. Zhai, S. Yang and G. Xu, *ACS Appl. Mat. Interfaces,* 2013, **5**, 3071-3074.
17. Z. Zhou, M. Žabèík, P. Lošták and C. Uher, *J. Appl. Phys.,* 2006, **99**, 043901.

18. X. Guo, J. Qin, X. Lv, L. Deng, X. Jia, H. Ma and H. Jia, *RSC Adv.*, 2016, **6**, 62430-62445.
19. Y. Pan, T.-R. Wei, C.-F. Wu and J.-F. Li, *J. Mater. Chem. C*, 2015, **3**, 10583-10589.
20. B. Wiendlocha, *J. of Electron. Mater.,* 2016, **45**, 3515-3531.
21. F. Hao, P. Qiu, Q. Song, H. Chen, P. Lu, D. Ren, X. Shi and L. Chen, *Materials*, 2017, **10**, 251.
22. G. E. Lee, I. H. Kim, Y. S. Lim, W. S. Seo, B. J. Choi and C. W. Hwang, *J. Korean Phys. Soc.*, 2014, **65**, 696-701.
23. F. Hao, P. Qiu, Y. Tang, S. Bai, T. Xin, H. S. Chu, Q. Zhang, P. Lu, T. Zhang and D. Ren, *Energy Environ. Sci.*, 2016, **9**, C6EE02017H.
24. B. Xu, M. T. Agne, T. Feng, T. C. Chasapis, X. Ruan, Y. Zhou, H. Zheng, J. H. Bahk, M. G. Kanatzidis, G. J. Snyder and Y. Wu, *Adv. Mater.*, 2017, **29**, 1605140.
25. B. Cheng, L. Wu, S. K. Kushwaha, R. J. Cava and N. P. Armitage, *Phys. Rev. B.* 2016, **94**, 201117.
26. B. Poudel, Q. Hao, Y. Ma, Y. Lan, A. Minnich, B. Yu, X. Yan, D. Wang, A. Muto, D. Vashaee, X. Chen, J. Liu, M. S. Dresselhaus, G. Chen and Z. Ren, *Science*, 2008, **320**, 634-638.
27. S. Wang, W. Xie, H. Li and X. Tang, *Intermetallics*, 2011, **19**, 1024-1031.
28. X. Tang, W. Xie, H. Li, W. Zhao, Q. Zhang and M. Niino, *Appl. Phys. Lett.*, 2007, **90**, 012102.
29. W. Xie, X. Tang, Y. Yan, Q. Zhang and T. M. Tritt, *Appl. Phys. Lett.*, 2009, **94**, 102111.
30. Y. Pan and J.-F. Li, *NPG Asia Mater.*, 2016, **8**, e275.
31. L. Hu, T. Zhu, X. Liu and X. Zhao, *Adv. Funct. Mater.*, 2014, **24**, 5211-5218.
32. Y. Pan, T.-R. Wei, C.-F. Wu and J.-F. Li, *J. Mater. Chem. C*, 2015, **3**, 10583-10589.
33. Y. Qiu, L. Xi, X. Shi, P. Qiu, W. Zhang, L. Chen, J. R. Salvador, J. Y. Cho, J. Yang, Y.-C. Chien, S.-W. Chen, Y. Tang and G. J. Snyder, *Adv. Funct. Mater.*, 2013, **23**, 3194-3203.
34. Y. Tang, Y. Qiu, L. Xi, X. Shi, W. Zhang, L. Chen, S.-M. Tseng, S.-w. Chen and G. J. Snyder, *Energy Environ. Sci.*, 2014, **7**, 812-819.
35. T. Zhang, K. Zhou, X. F. Li, Z. Q. Chen, X. L. Su and X. F. Tang, *J. Appl. Phys.,* 2015, **117**, 055103. **117**, 055103.
36. H. F. He, Z. Q. Chen, Y. Zheng, D. W. Yang, and X. F. Tang, *J. Phys. Chem. C*, 2014, **118**, 22389-22394.
37. W. Zheng, D. Yang, P. Bi, C. He, F. Liu, J. Shi, Y. Ding, Z. Wang and R. Xiong, *J. Electron. Mater.*, 2016, **46**, 2936-2943.
38. L. D. Zhao, S. H. Lo, J. He, H. Li, K. Biswas, J. Androulakis, C. Wu, T. P. Hogan, D. Y. Chung and V. P. Dravid, *J. Am. Chem. Soc.*, 2011, **133**, 20476-20487.
39. J. Callaway, *Phys. Rev.,* 1959, **113**, 436-441.
40. J. Callaway and H. C. Von Baeyer, *Phys. Rev.,* 1960, **120**, 1149-1154.
41. C. W. Nan, R. Birringer, D. R. Clarke and H. Gleiter, *J. Appl. Phys.*, 1997, **81**, 6692-6699.
42. H. Xie, X. Su, G. Zheng, T. Zhu, K. Yin, Y. Yan, C. Uher, M. G. Kanatzidis and X. Tang, *Adv. Energy Mater.*, 2017, **7**, 1601299.43.
43. D. G. Cahill, S. K. Watson and R. O. Pohl, Phys. Rev. B: Condensed Matter., 1992, 46, 6131.
44. X. Su, P. Wei, H. Li, W. Liu, Y. Yan, P. Li, C. Su, C. Xie, W. Zhao, P. Zhai, Q. Zhang, X. Tang and C. Uher, *Adv. mater.*, 2017, **29**, 1602013.
45. X. Su, F. Fu, Y. Yan, G. Zheng, T. Liang, Q. Zhang, X. Cheng, D. Yang, H. Chi, X. Tang, Q. Zhang and C. Uher, *Nat. commun.*, 2014, **5**, 4908.
46. G. Tan, F. Shi, S. Hao, L. D. Zhao, C. Hang, X. Zhang, C. Uher, C. Wolverton, V. P. Dravid and M. G. Kanatzidis, *Nat. commun.*, 2016, **7**, 12167.
47. H.-S. Kim, N. A. Heinz, Z. M. Gibbs, Y. Tang, S. D. Kang and G. J. Snyder, *Mater.Today*, 2017, **20**,

452-459.
48. Y. Li, Y. Dou, X. Qin, J. Zhang, H. Xin, D. Li, C. Song, T. Zou, Y. Liu and C. Li, *RSC Adv.*, 2016, **6**, 12243-12248.
49. Y. Zheng, G. Tan, Y. Luo, X. Su, Y. Yan and X. Tang, *Materials (Basel)*, 2017, **10**, 617.
50. Y. Zheng, Q. Zhang, X. Su, H. Xie, S. Shu, T. Chen, G. Tan, Y. Yan, X. Tang, C. Uher and G. J. Snyder, *Adv. Energy Mater.*, 2015, **5**, 1401391.
51. J. P. Perdew, K. Burke and M. Ernzerhof, *Phys. Rev. Lett.*, 1996, **78**, 3865.
52. G. Kresse and J. Furthmüller, *Phys. Rev. B: Condens. Matter*, 1996, **54**, 11169.
53. W. M. YIM and F. D. ROSI, *Solid-State Ekcrronics*, 1972, **15, pp.**, 1121- 1140.
54. A. Zunger, S. Wei, L. G. Ferreira and J. E. Bernard, *Phys. Rev. Lett.*, 1990, **65**, 353-356.

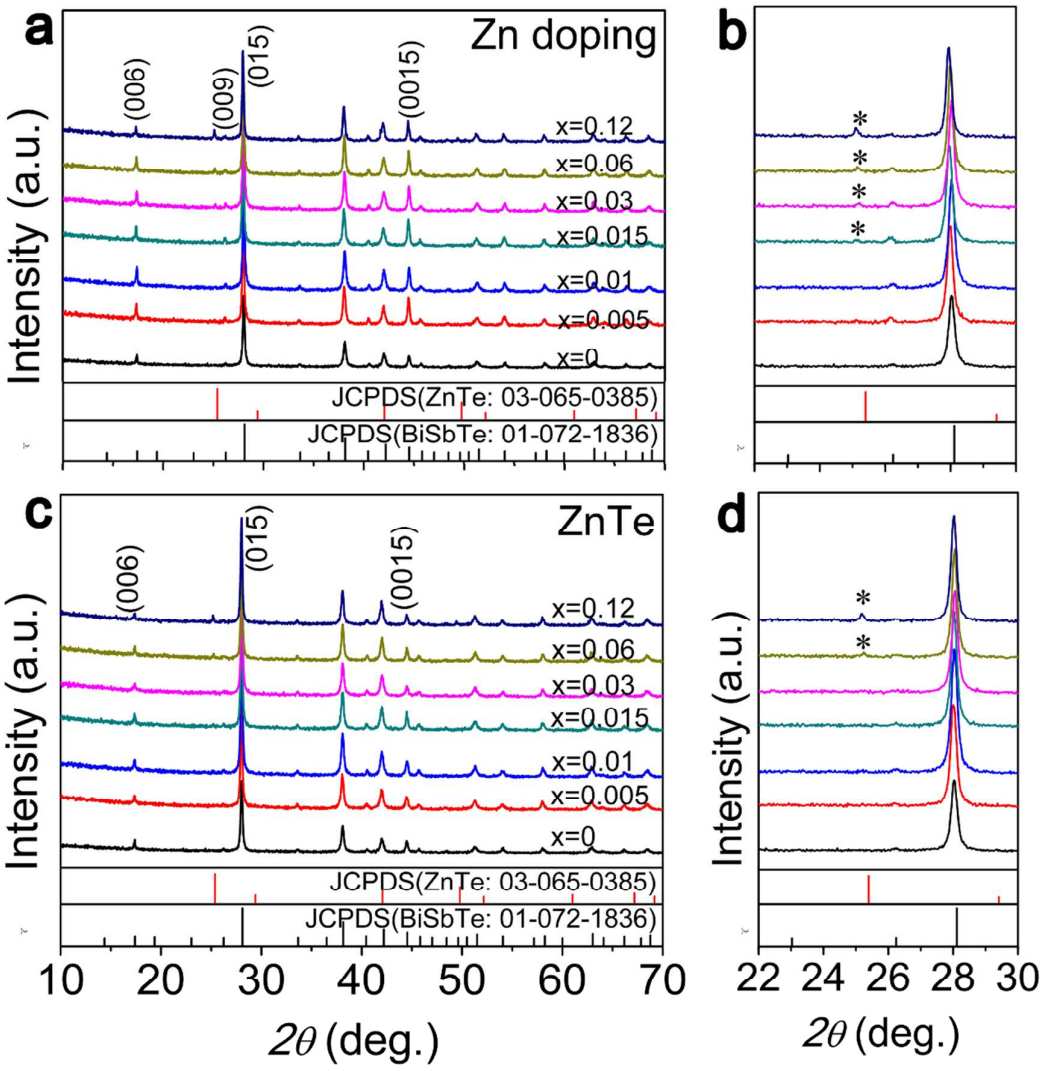

Figure 1: (a) X-ray diffraction (XRD) patterns of powdered $Zn_x(Bi_{0.46}Sb_{1.54})_{1-x/2}Te_3$ prior to SPS. (b) Expanded view of (a) for angles between 22° and 30°. (c) X-ray diffraction patterns of powdered $Zn_xBi_{0.46}Sb_{1.54}Te_{3+x}$ prior to SPS and (d) its expanded view for angles between 22° and 30°.

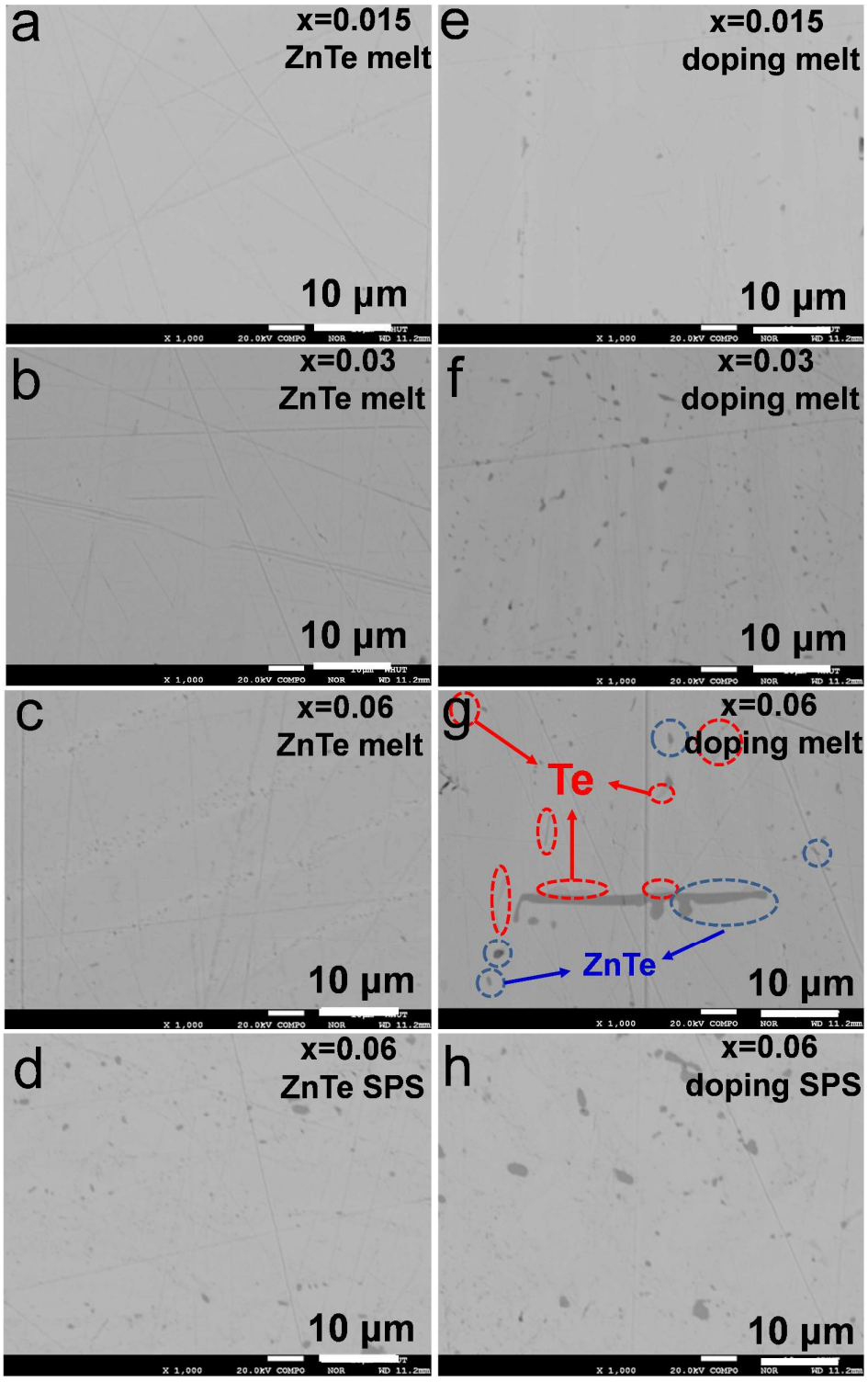

Figure 2: Back scattered electron images of polished surfaces of $Zn_xBi_{0.46}Sb_{1.54}Te_{3+x}$ ingots before SPS: (a) x=0, (b) x=0.03, (c) x=0.06, and (d) sintered bulk of $Zn_{0.06}Bi_{0.46}Sb_{1.54}Te_{3.06}$. Back scattered electron images of polished surfaces for $Zn_x(Bi_{0.46}Sb_{1.54})_{1-x/2}Te_3$ ingots before SPS: (e) x=0.015, (f) x=0.03, (g) x=0.06, and (h) sintered bulk for x=0.06.

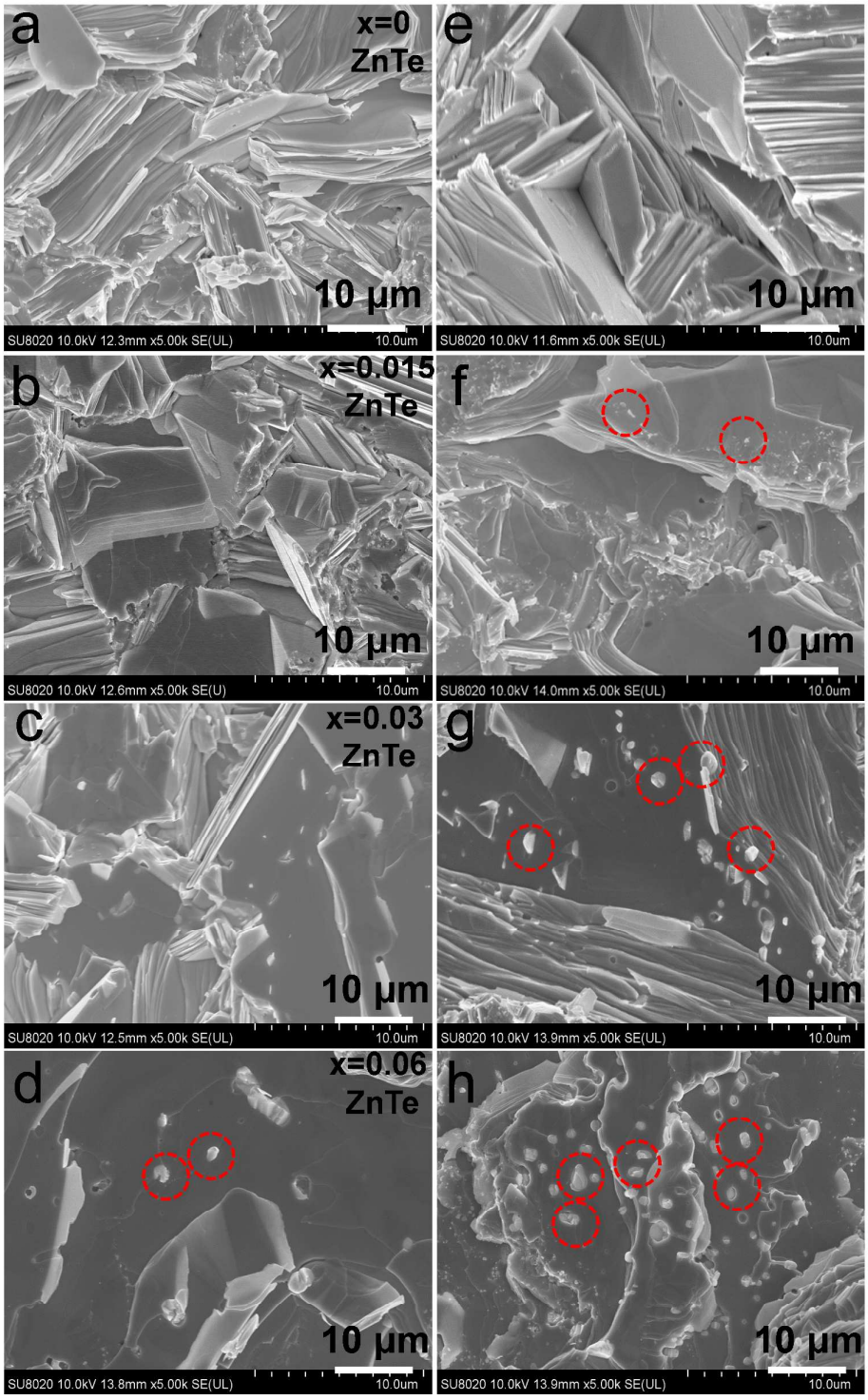

Figure 3: Field emission scanning electron microscope images of fracture surfaces of sintered samples of $Zn_xBi_{0.46}Sb_{1.54}Te_{3+x}$: (a) x=0, (b) x=0.015, (c) x=0.03, (d) x=0.06. Field emission scanning electron microscope images of fracture surfaces of sintered samples of $Zn_x(Bi_{0.46}Sb_{1.54})_{1-x/2}Te_3$: (e) x=0.005, (f) x=0.015, (g) x=0.03, (h) x=0.06. Second phases are marked by red-dashed circles.

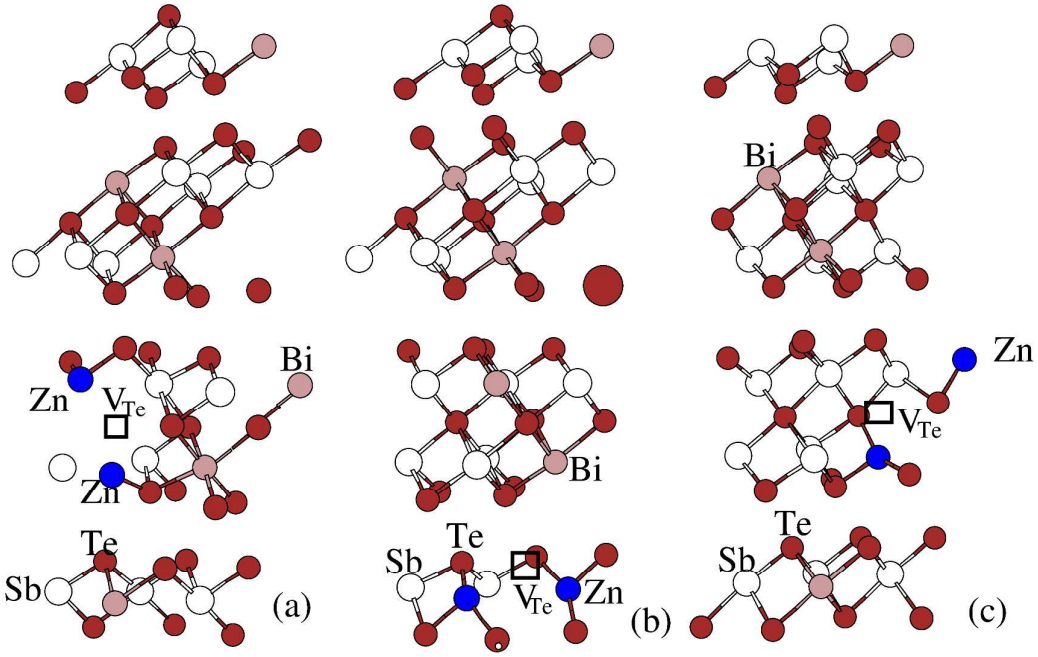

Figure 4: The most favorable structures of (a) $Sb_{16}Bi_6Te_{35}Zn_2$ corresponding complex defect of $2Zn_{Sb}+V_{Te}$ with the formation energy difference of -0.41 eV/complex, (b) $Sb_{17}Bi_5Te_{35}Zn_2$ corresponding complex defect of $Zn_{Sb}+Zn_{Bi}+V_{Te}$ (-0.32 eV/complex), and (c) $Sb_{18}Bi_4Te_{35}Zn_2$ corresponding complex defect of $2Zn_{Bi}+V_{Te}$ (-0.31 eV/complex). Here the formation energy difference is the complex formation energy relative to the isolated defect formation energies. The absolute complex formation energy themselves are given in Table 1.

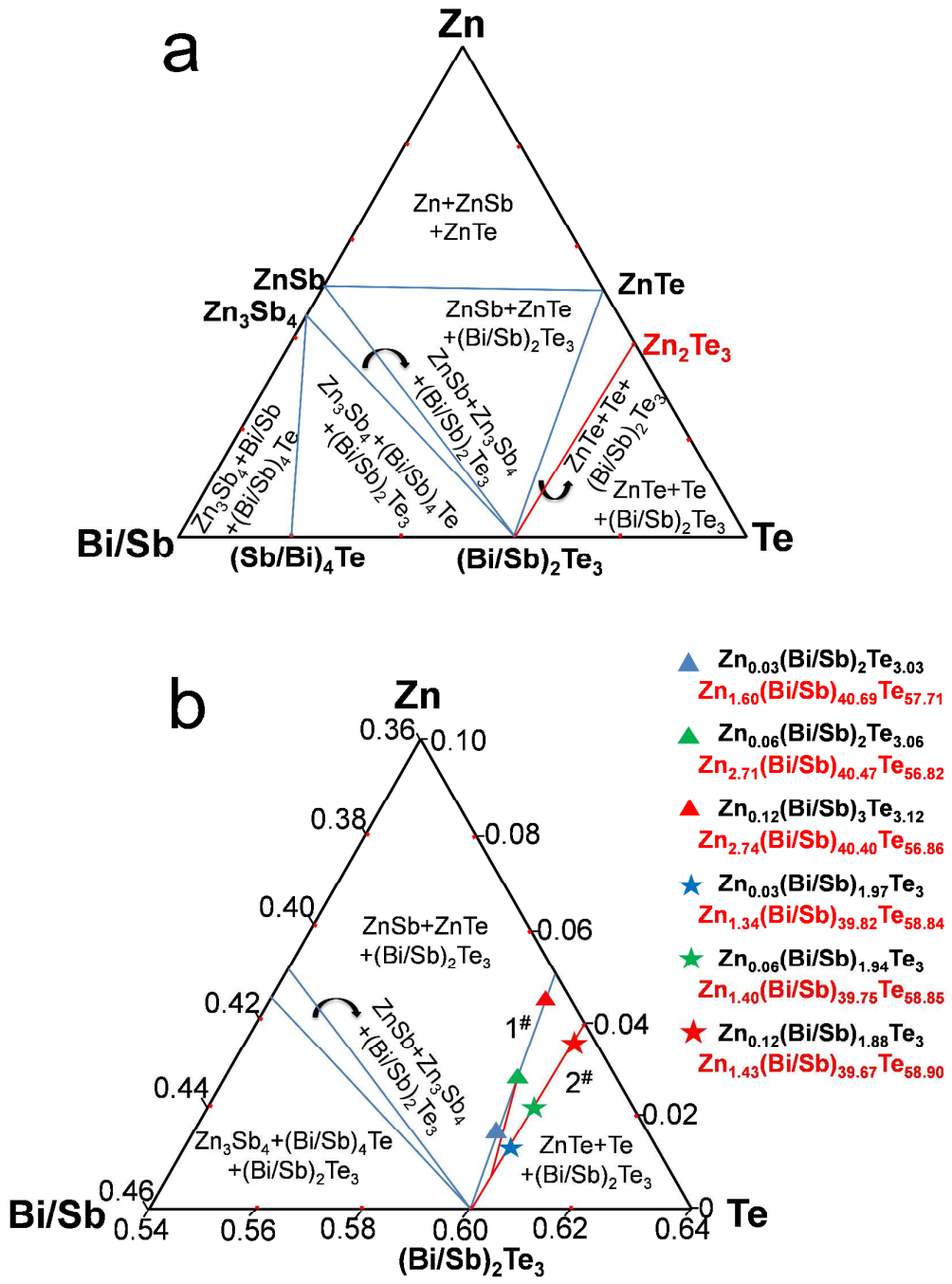

Figure 5: Proposed phase diagram for Zn-containing $(Bi/Sb)_2Te_3$ at 673 K. (a) Full diagram with related binary phases. (b) The enlarged region of the phase diagram near $(Bi/Sb)_2Te_3$. The red lines do not really exist, they are drawn to facilitate the interpretation of this part. Solid symbols represent the composition of the $(Bi/Sb)_2Te_3$ majority phase using the experimental EPMA value for samples with nominally incorporated ZnTe (marked by triangles) and for Zn-doped samples (marked by asterisks), respectively.

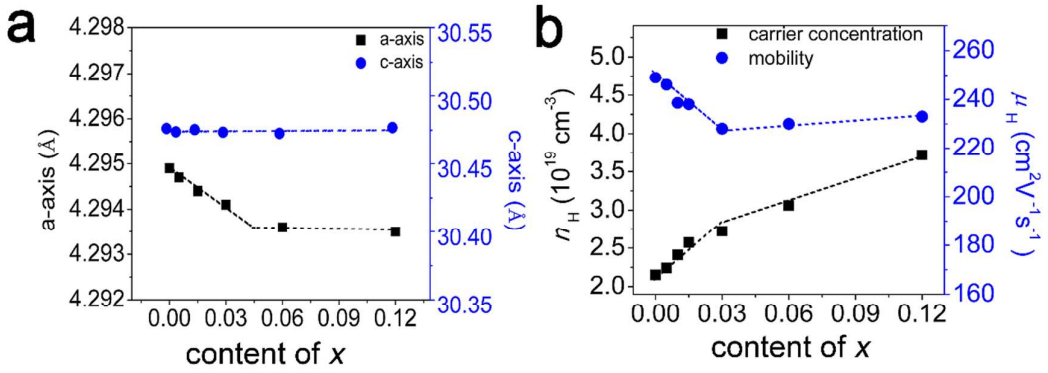

Figure 6: (a) Lattice parameters and (b) room temperature carrier concentration n_H and mobility μ_H for $Zn_xBi_{0.46}Sb_{1.54}Te_{3+x}$ samples.

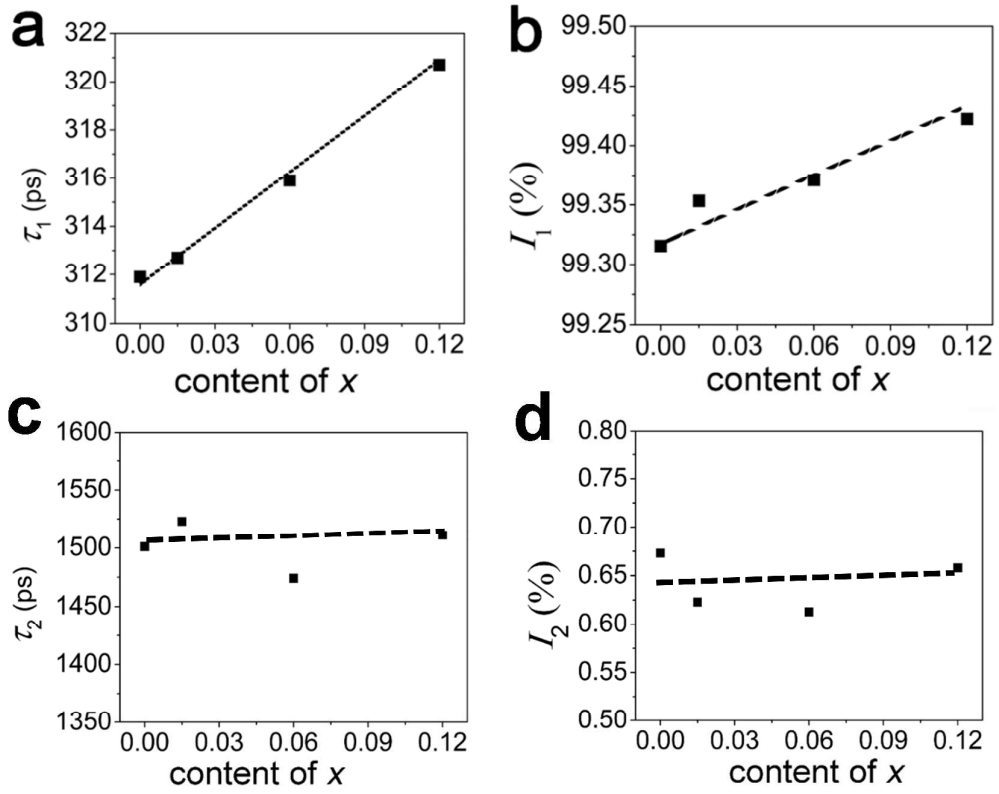

Figure 7: (a) and (b) Variation of positron lifetime τ_1 and intensity I_1 for $Zn_xBi_{0.46}Sb_{1.54}Te_{3+x}$ samples. (c) and (d) Variation of positron lifetime τ_2 and intensity I_1 for $Zn_xBi_{0.46}Sb_{1.54}Te_{3+x}$ samples.

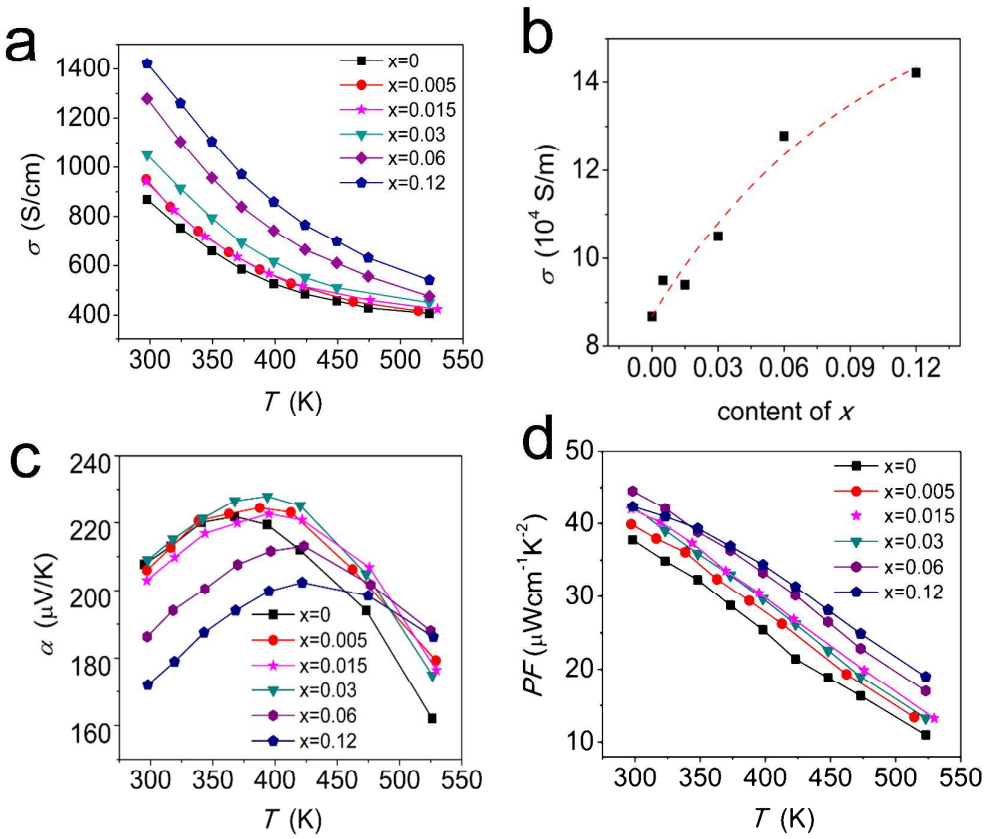

Figure 8: Temperature dependence of (a) the electrical conductivity, (c) the Seebeck coefficients, and (d) the power factor of $Zn_xBi_{0.46}Sb_{1.54}Te_{3+x}$ samples. (b) Relationship between the ZnTe content and the room temperature electrical conductivity.

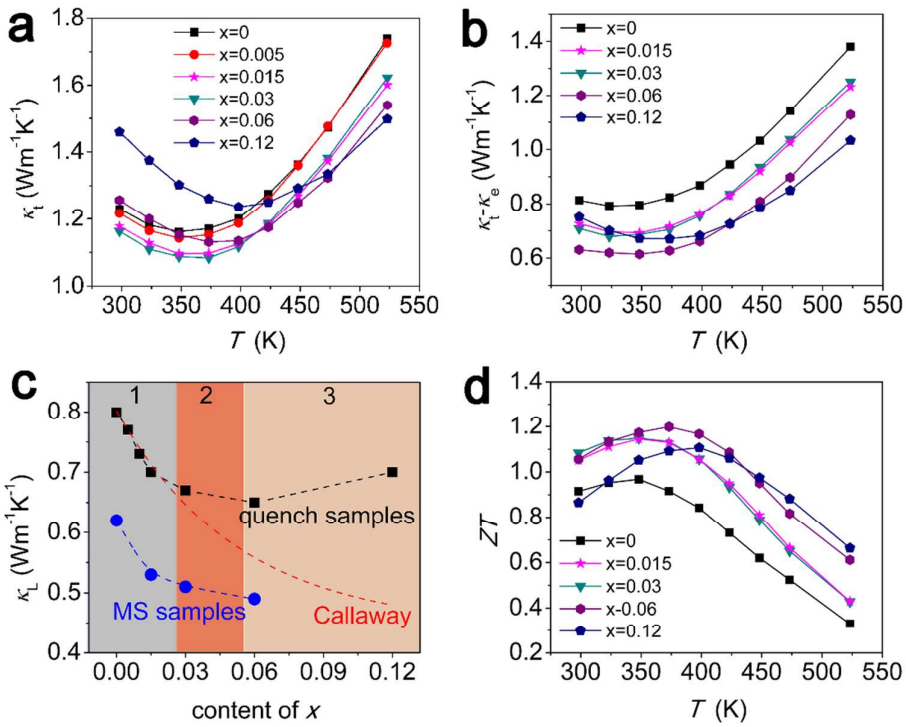

Figure 9: Temperature dependence of (a) the total thermal conductivity, (b) κ-κ_e, and (c) the *ZT* value for $Zn_xBi_{0.46}Sb_{1.54}Te_{3+x}$ samples. (d) Relationships between the ZnTe content and the room temperature lattice thermal conductivity. The lattice thermal conductivity based on the Callaway model is shown by a dashed red curve.

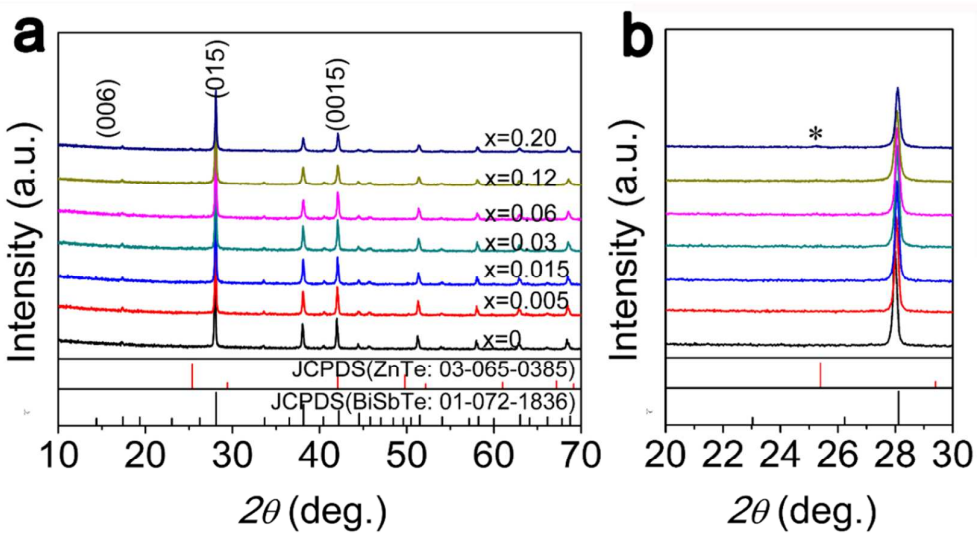

Figure 10: (a) Powder XRD patterns of melt-spun ribbons of $Zn_xBi_{0.46}Sb_{1.54}Te_{3+x}$. (b) Expanded view of (a) between angles 20° and 30°. The asterisk indicates the presence of the ZnTe secondary phase in a sample with x = 0.20.

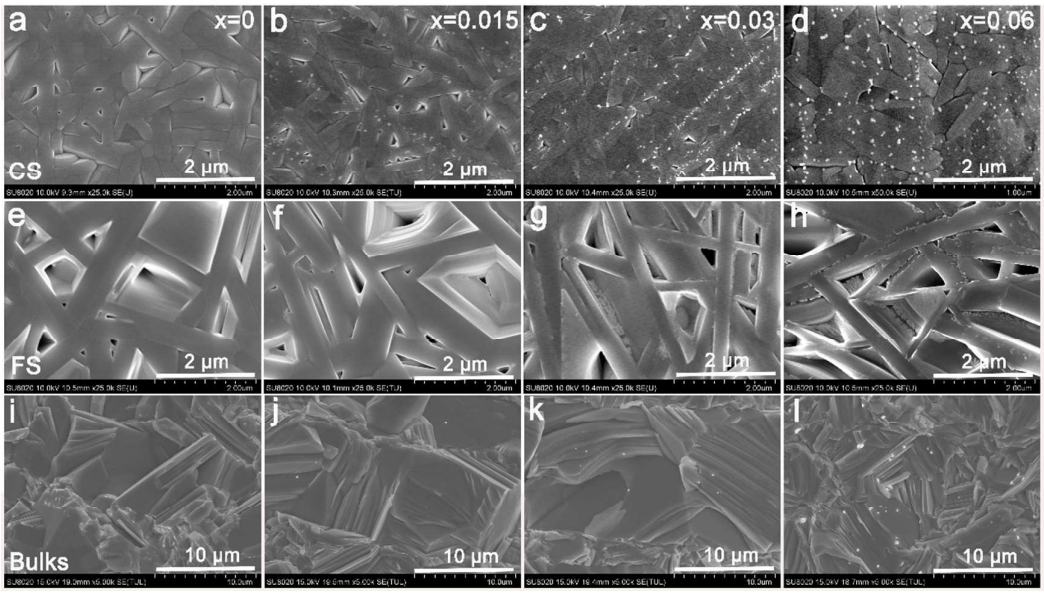

Figure 11: FESEM images of (a-d) the contact surface (CS) and (e-h) free surface (FS) of melt-spun ribbons and (i-l) fracture surfaces of SPS-sintered bulk samples of $Zn_xBi_{0.46}Sb_{1.54}Te_{3+x}$: (a), (e) and (i) x=0, (b), (f) and (j) x=0.015, (c), (g) and (k) x=0.03, (d), (h) and (l) x=0.06.

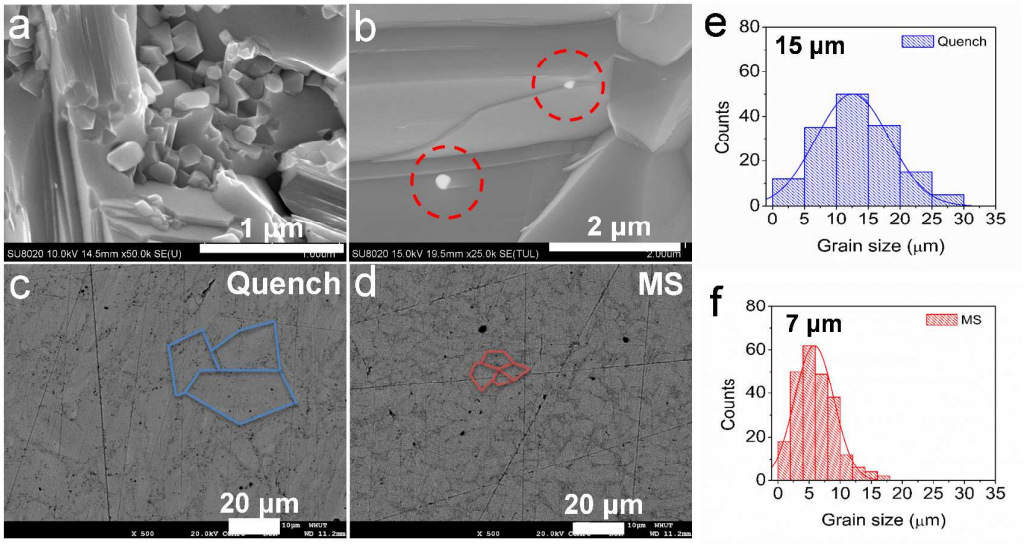

Figure 12: (a) and (b) FESEM images of fracture surfaces of sintered bulk sample of $Zn_{0.06}Bi_{0.46}Sb_{1.54}Te_{3.06}$, ZnTe secondary phases are marked by red-dashed circles. (c) Back scattered electron images of polished surfaces of sample prepared by traditional method and (e) its grain size distribution. (d) Back scattered electron images of polished surfaces of sample prepared by melting spinning and (f) its grain size distribution.

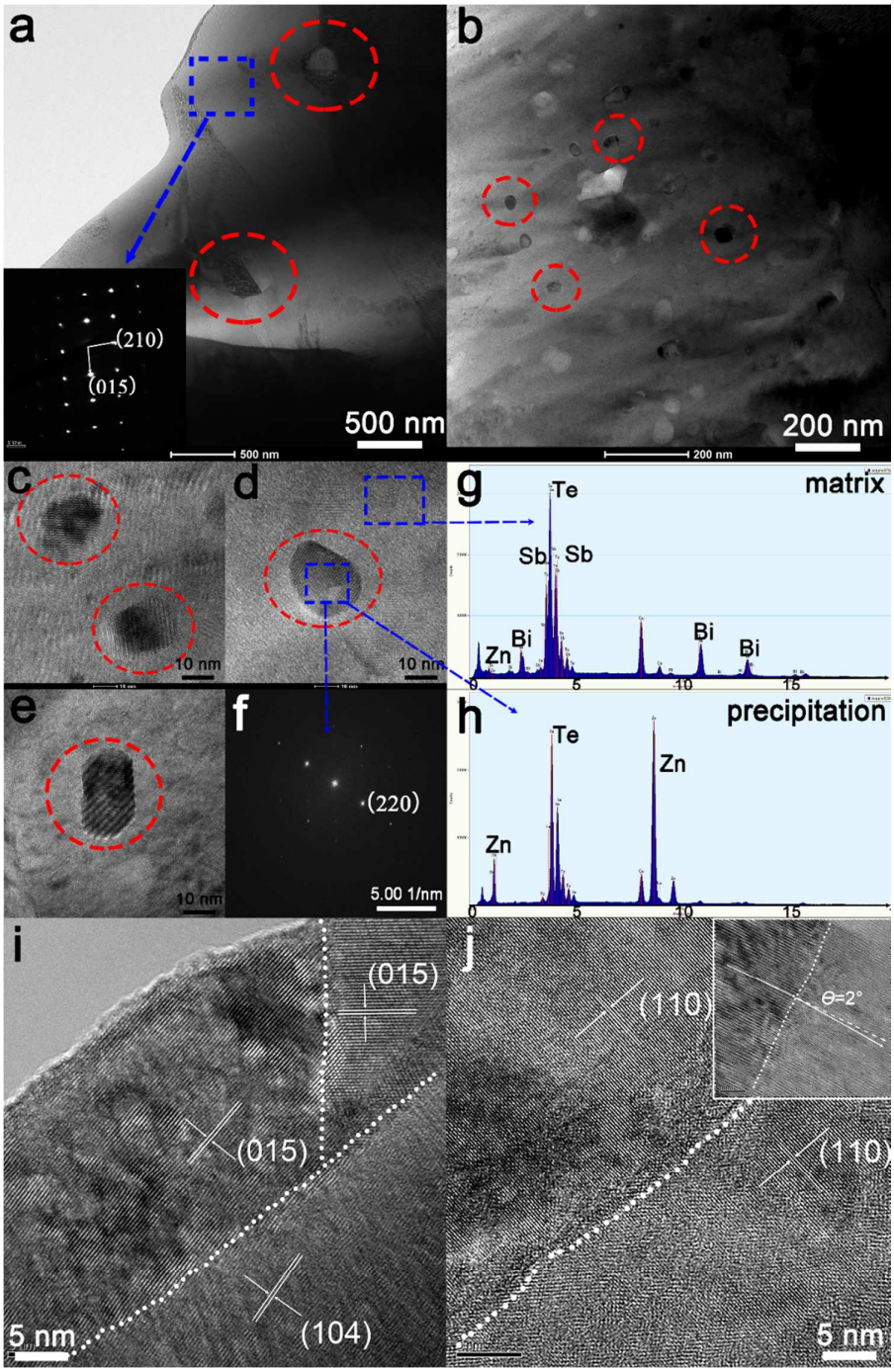

Figure 13: (a-b) TEM images and (c-e) HRTEM images of the melt-spun $Zn_{0.06}Bi_{0.46}Sb_{1.54}Te_{3.06}$ sample after SPS with nanoparticles marked by red dashed circles. The inset of (a) shows selected area electron diffraction (SEAD) of a narrow region (blue dashed rectangle) corresponding to the $Bi_{0.46}Sb_{1.54}Te_3$ matrix. (f) An FFT image of the secondary phase (delineated by a red dashed circle in Figure 12(d)). (g-h) EDS patterns of the matrix and nano-precipitates, (i) distinct grain boundaries between nanoparticles, (j) perfect alignment between two $Bi_{0.46}Sb_{1.54}Te_3$ grains, the inset gives another example of a low-angle boundary.

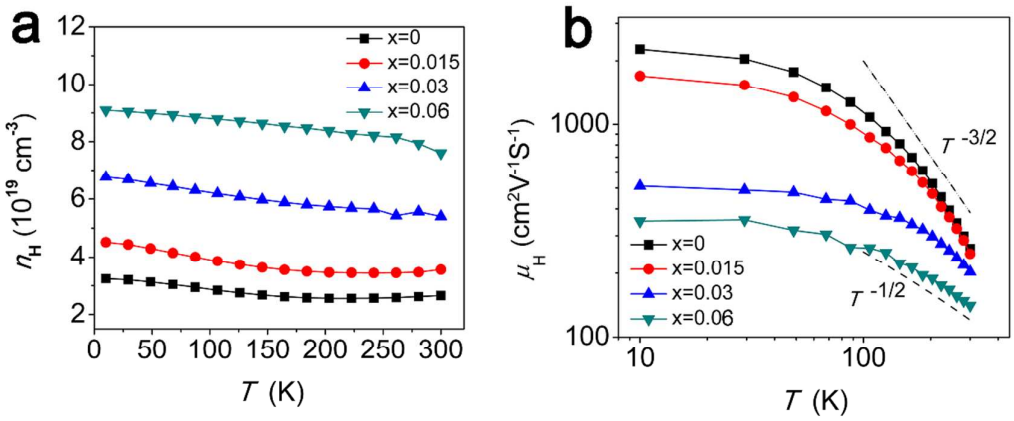

Figure 14: Temperature dependence (10 K-300 K) of (a) the carrier concentration and (b) the carrier mobility for melt-spun $Zn_xBi_{0.46}Sb_{1.54}Te_{3+x}$ samples after SPS.

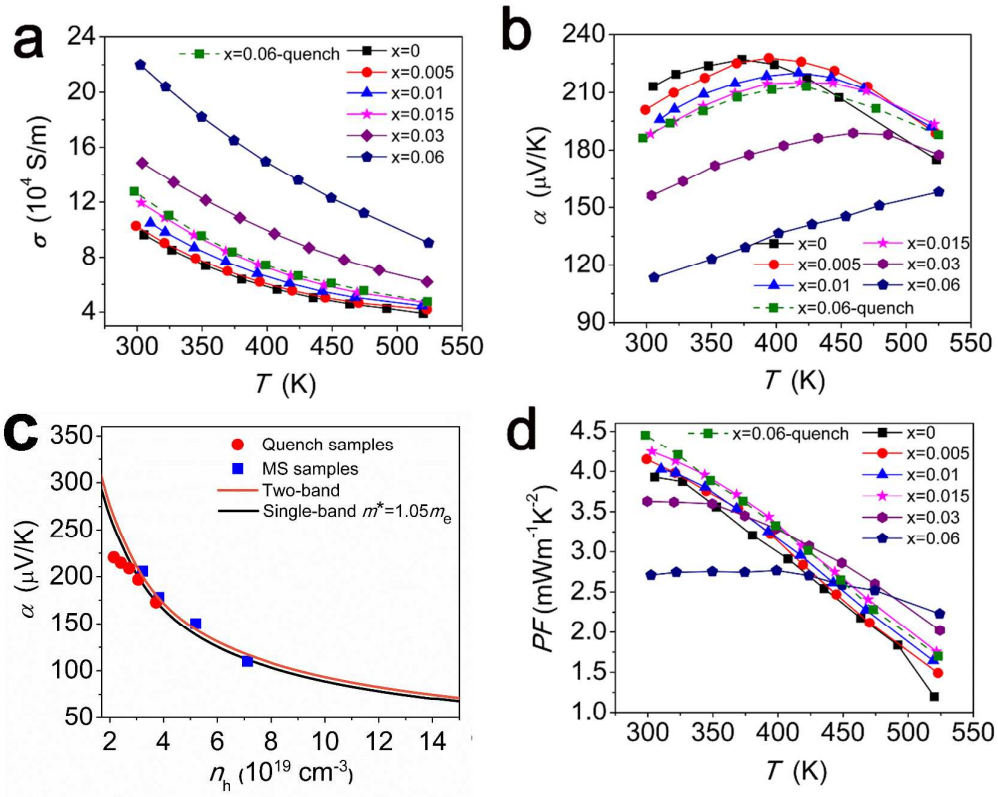

Figure 15: Temperature dependence of (a) the electrical conductivity, (b) the Seebeck coefficients, and (c) Pisarenko plot for melt-spun samples with different ZnTe content. (d) the power factor for the melt-spun $Zn_xBi_{0.46}Sb_{1.54}Te_{3+x}$ samples after SPS.

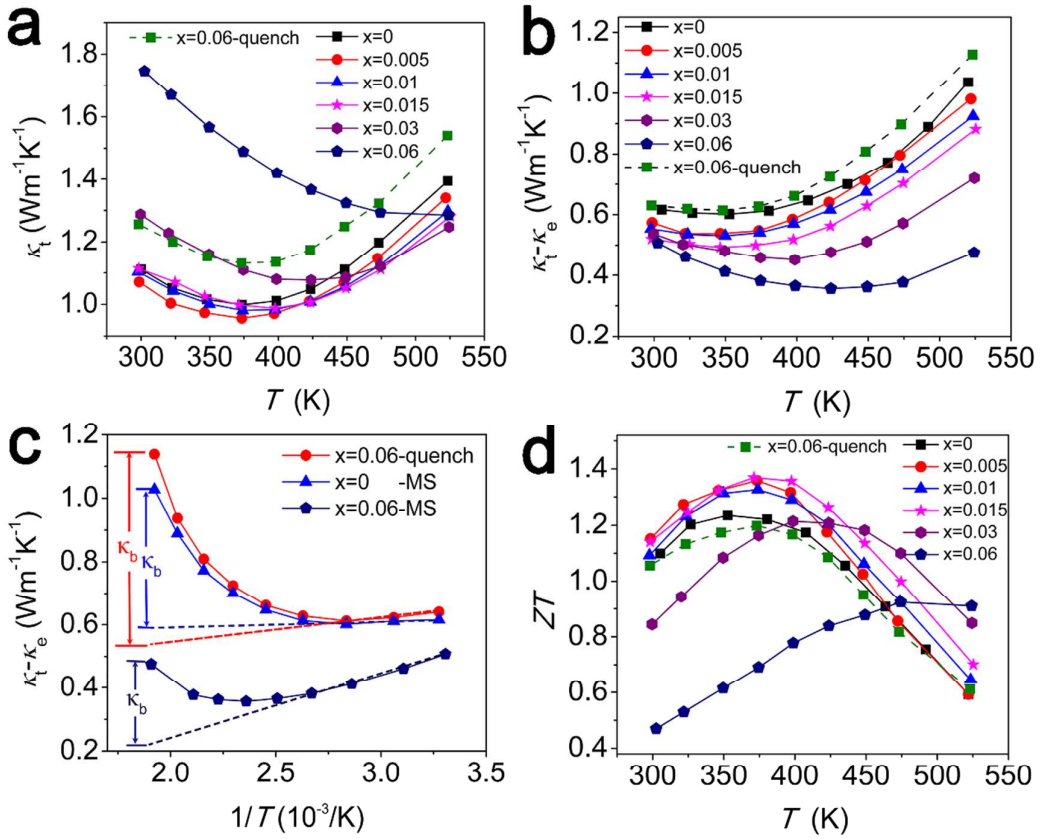

Figure 16: (a) Temperature dependence of the total thermal conductivity, κ_t. (b) Temperature dependence of the κ_t-κ_e term. (c) Variation of $\kappa_t - \kappa_e$ with the reciprocal temperature. Deviations of the thermal conductivity from the straight lines indicate a significant bipolar contribution. (d) Temperature dependence of the dimensionless thermoelectric figure of merit *ZT* for the melt-spun $Zn_xBi_{0.46}Sb_{1.54}Te_{3+x}$ samples after SPS.

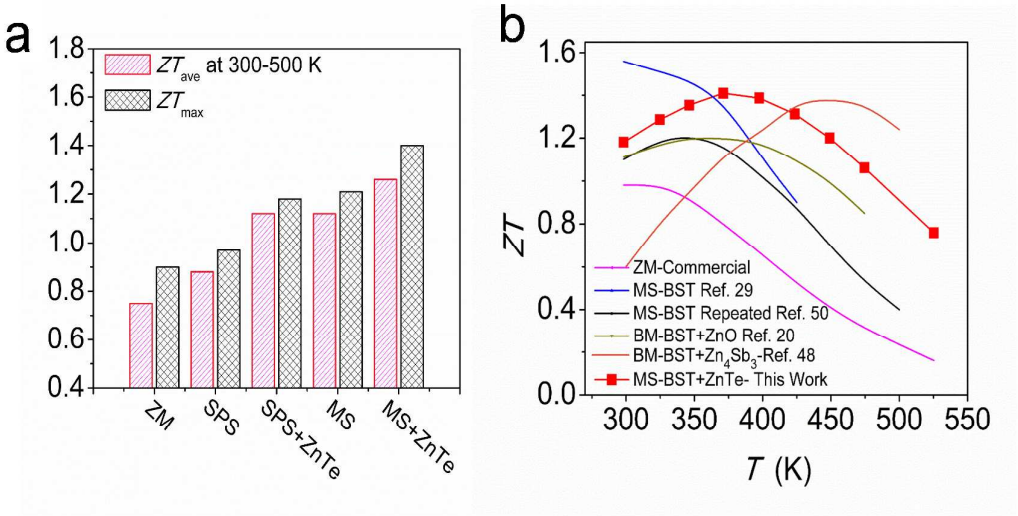

Figure 17: (a) Comparison of ZT_{max} and ZT_{ave} values for different samples. (b) Comparison of ZT values for different works.

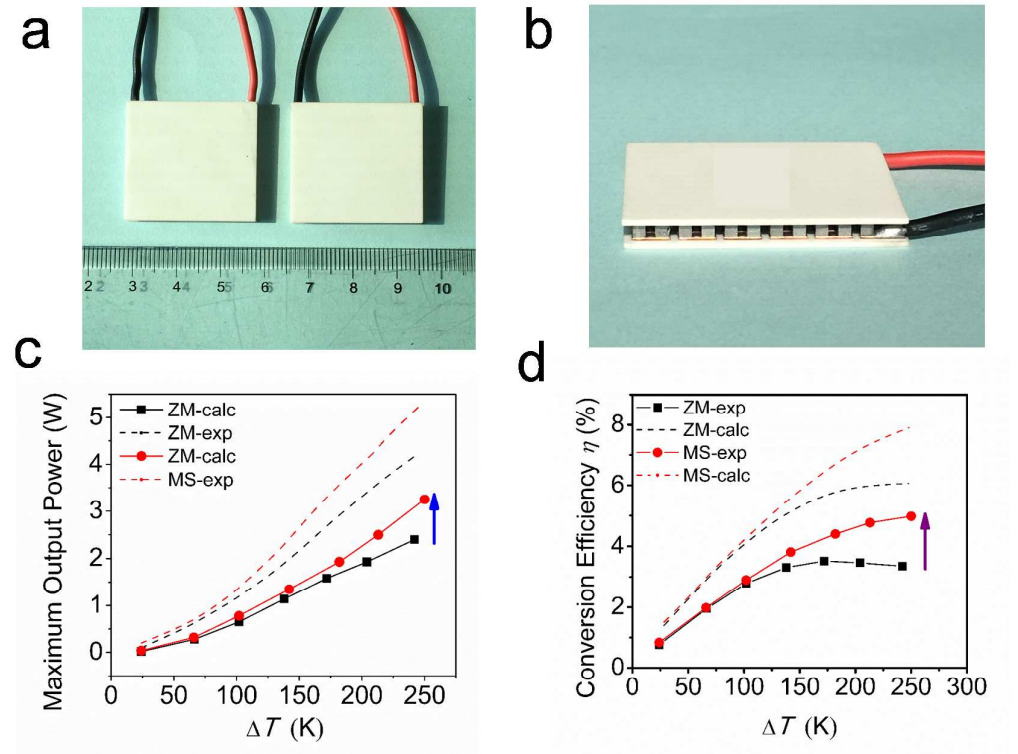

Figure 18: (a) and (b) Images of fabricated thermoelectric modules. (c) Output power and (d) conversion efficiency of modules. The dashed lines represent theoretical output power or energy conversion efficiency for the modules, the solid lines represent the experimental output power or energy conversion efficiency for the modules.

Table 1: Formation energy of different complex configurations. The configurations are listed in different compositions with corresponding defect complex marked in parenthesis. The formation energy is in eV/complex. The numbers in red are formation energy difference relative to isolated defects. The numbers in parenthesis are the absolute values of formation energy. The total energies of each species in bulk form are adopted as corresponding chemical potentials for absolute formation energy calculations.

Config.	$Sb_{16}Bi_6Te_{35}Zn_2$ ($2Zn_{Sb}+V_{Te}$)	$Sb_{16}Bi_6Te_{35}Zn_2$ ($2Zn_{Sb}+V_{Te}$)	$Sb_{16}Bi_6Te_{35}Zn_2$ ($2Zn_{Sb}+V_{Te}$)	$Sb_{16}Bi_6Te_{35}Zn_2$ ($2Zn_{Sb}+V_{Te}$)
E_{form}	-0.05 (0.69)	-0.28 (0.47)	-0.36 (0.29)	-0.41 (0.24)
Config.	$Sb_{17}Bi_5Te_{35}Zn_2$ ($Zn_{Sb}+Zn_{Bi}+V_{Te}$)	$Sb_{17}Bi_5Te_{35}Zn_2$ ($Zn_{Sb}+Zn_{Bi}+V_{Te}$)	$Sb_{18}Bi_4Te_{35}Zn_2$ ($2Zn_{Bi}+V_{Te}$)	$Sb_{18}B_4Te_{35}Zn_2$ ($2Zn_{Bi}+V_{Te}$)
E_{form}	-0.28 (0.55)	-0.32 (0.51)	-0.19 (0.73)	-0.31 (0.61)

Table 2: Disorder scattering parameters Γ_M, Γ_S, Γ, strain field-related adjustable parameter ε_1, disorder scaling parameter u, and the calculated lattice thermal conductivity for samples with different ZnTe content.

compounds	Γ_m 10^{-3}	Γ_S 10^{-3}	Γ 10^{-3}	ε_1	u	κ_L-calc $Wm^{-1}K^{-1}$
x=0						0.80
x=0.005	0.064	17.236	17.300	174	0.347	0.77
x=0.01	0.126	39.084	39.210	183	0.503	0.74
x=0.015	0.187	71.013	71.200	191	0.625	0.72
x=0.03	0.368	92.132	92.500	200	0.941	0.64
x=0.06	0.731	128.269	129.000	256	1.255	0.56
x=0.12	1.458	95.242	96.700	348	1.998	0.42

Table 3: Room temperature physical parameters of samples with different content of ZnTe.

compounds	σ 10^4 Sm^{-1}	α μVK^{-1}	n_H 10^{-3}	μ cm^{2}V^{-1}s^{-1}	m^*/m_e
MS x=0	9.80	210	3.22	195	1.06
MS x=0.015	12.20	185	3.75	203	1.03
MS x=0.03	15.60	154	5.20	181	1.08
MS x=0.06	22.20	119	7.11	140	1.02
quench x=0	8.70	222	2.22	249	0.98
quench x=0.015	9.60	216	2.41	242	0.99
quench x=0.3	10.70	209	2.72	238	0.99
quench x=0.06	12.80	199	3.16	236	1.01
quench x=0.12	14.20	176	3.72	232	1.02